Geophysical Journal International

Geophys. J. Int. (2019) **218,** 247–267
Advance Access publication 2019 March 16
GJI Geodynamics and tectonics

doi: 10.1093/gji/ggz139

Controls on the geometry and evolution of thin-skinned fold-thrust belts, and applications to the Makran accretionary prism and Indo–Burman Ranges

Thomasina V. Ball,[1,2] Camilla E. Penney,[3] Jerome A. Neufeld[1,2,4] and Alex C. Copley[3]

[1] *Bullard Laboratories, Department of Earth Sciences, University of Cambridge, Madingley Road, Cambridge CB3 0EZ, UK. E-mail: tvb21@cam.ac.uk*
[2] *BP Institute, University of Cambridge, Madingley Road, Cambridge CB3 0EZ, UK*
[3] *COMET, Bullard Laboratories, Department of Earth Sciences, University of Cambridge, Madingley Road, Cambridge CB3 0EZ, UK*
[4] *Department of Applied Mathematics and Theoretical Physics, University of Cambridge, CMS Wilberforce Road, Cambridge CB3 0WA, UK*

Accepted 2019 March 14. Received 2019 February 18; in original form 2018 September 4

SUMMARY

The formation of fold-thrust belts at convergent margins is a dynamic process. Accretion of weak sediments to the front of the overriding plate results in crustal thickening and continued flexural subsidence of the underthrusting plate. Fold-thrust belts are often treated as a Coulomb wedge having self-similar geometries with a critical taper, and either a rigid or isostatically compensated base. In this paper, we build upon this work by developing a new dynamic model to investigate both the role of the thickness and material properties of the incoming sediment, and the flexure in the underthrusting plate in controlling the behaviour and evolution of fold-thrust belts. Our analysis shows that the evolution of fold-thrust belts can be dominated by either gravitational spreading or vertical thickening, depending on the relative importance of sediment flux, material properties and flexure. We apply our model to the Makran accretionary prism and the Indo–Burman Ranges, and show that for the Makran flexure must be considered in order to explain the dip of the sediment–basement interface from seismic reflection profiles. In the Indo–Burman Ranges, we show that incoming sediment thickness has a first-order control on the variations in the characteristics of the topography from north to south of the Shillong Plateau.

Key words: Continental margins: convergent; Dynamics: gravity and tectonics; Lithospheric flexure; Mechanics, theory and modelling.

1 INTRODUCTION

A wide range of geometries of mountain ranges are formed by plate convergence. The sizes and thermal structures of these ranges control their rheology, and therefore their deformation and evolution. At one extreme, the largest ranges on the Earth (e.g. the Tibetan Plateau and the Andes) involve the entire thickness of the lithosphere, are bounded by rigid plates that are thousands of kilometres apart and involve a range of deformation mechanisms including seismic failure in earthquakes and thermally activated creep (e.g. Brace & Kohlstedt 1980; Chen & Molnar 1983). Opinion is divided in terms of the relative dynamical importance of brittle deformation on faults and the more distributed deformation in the underlying ductile lithosphere, and in the choice of boundary conditions used on the base and lateral edges for models of mountain ranges (e.g. Molnar & Tapponnier 1975; England & McKenzie 1982; Beaumont *et al.* 2001; Meade 2007; Flesch *et al.* 2018). In this paper, we examine the behaviour of smaller ranges over length scales of 100s of km. At some convergent margins, weak sediments on an underthrusting plate are deformed during accretion to the front of a relatively rigid 'backstop', which represents a region of the overlying plate that is stronger than the incoming sediments. This leads to the formation of a fold-thrust belt, or an accretionary wedge, which is our focus here.

We examine a coupled system of deformation of the incoming sediment pile and flexure of the underthrusting plate. By developing new dynamic models, we are able to address the role that is played by the thickness and material properties of the incoming sediments, and by the elastic properties of the underthrusting plate, in the behaviour and evolution of fold-thrust belts. First, we describe the effects of changing these physical parameters on the geometry and deformation of the resulting fold-thrust belts. We then describe applications to specific regions that demonstrate the geological implications of the effects we have studied. In particular, we consider the Makran accretionary prism in order to demonstrate the necessity of including flexure in the model. We then investigate how changing the sediment thickness affects the geometry of fold-thrust belts by considering the Indo–Burman Ranges.

2 PREVIOUS MODELS

Price (1973) was the first to model a wedge-like fold-thrust belt using a continuum plastic rheology where the yield strength is depth independent. In Price's model, flow is driven by horizontal pressure gradients associated with surface slopes. The continuum plastic model was revisited by Elliot (1976) and Chapple (1978). By setting the strength of the interface between the wedge and the rigid underthrusting plate to be that of the wedge, Elliot (1976) showed that the gravitational force provided by the weight of the accreted sediment dominated the deformation. Conversely, by introducing a weaker interface between the wedge and the underthrusting plate, Chapple (1978) highlighted that horizontal compression associated with shortening can contribute to overcoming the resisting shear stress at the base of the wedge without the requirement of a surface slope. The analysis of Elliot (1976) and Chapple (1978) was then expanded by Stockmal (1983) using slipline theory to calculate the stress and velocity field within the wedge.

Such models do not reflect that the material strength in a fold-thrust belt is expected to increase with depth due to the increasing effective overburden stress and lithification. Davis *et al.* (1983), Dahlen *et al.* (1984) and Dahlen (1984, 1990) used a Coulomb rheology, where the yield strength increases with depth and is set by the internal friction angle, for the case of a non-cohesive (Davis *et al.* 1983) or a cohesive (Dahlen *et al.* 1984) thrust belt. Extensions to these models have considered the effect of pore fluid pressures and changes in cohesion due to compaction and lithification (Zhao *et al.* 1986). In particular, Dahlen (1984) presented an exact solution for the stress state in a non-cohesive wedge.

The Coulomb wedge described by Davis *et al.* (1983) and others relies on the hypothesis that the interior of the wedge is everywhere on the verge of failure (Mandl 1988). Hence, this model does not account for the possibility that deformation may be confined to a narrow zone, as observed in many fold-thrust belts where deformation is dominated by large slip on a few major faults (Suppe 1980). Numerical models have been developed by others to allow for inhomogeneous deformation with more complex rheologies, including plastic (Borja & Dreiss 1989; Willett 1992), elasto-plastic (Simpson 2011) and elasto-visco-plastic (Stockmal *et al.* 2007; Ruh *et al.* 2012) rheologies, as well as for time-dependent stress states (e.g. Wang & Hu 2006).

Alongside these studies, fold-thrust belts have been described with more simplified rheologies. In thick layers of sediment, deformation is thought to be associated with diffusion creep due to water-assisted transport of material via diffusion at the grain scale, and is known to occur at low temperatures in sediments (Rutter 1983). Such a deformation mechanism would result in a viscous fluid rheology at large scales. Emerman & Turcotte (1983) first considered the geometry of a fold-thrust belt with a purely viscous rheology. Using lubrication theory (flow in a thin viscous layer), they described a quasi-steady profile due to the balance of advection of the incoming sediment layer and gravitational spreading within the wedge. Applying the model to bathymetric profiles across the Kurile, Ryukyu and Aleutian accretionary prisms, Emerman and Turcotte inferred sediment viscosities between 10^{17} and 10^{18} Pa s. A viscous rheology has also been used to investigate the asymmetry of doubly vergent orogens (Medvedev 2002), and to understand the length scales over which coupling to the kinematics of the underlying mantle is important (Ellis *et al.* 1995). More recently, Perazzo & Gratton (2010) demonstrated that the growth of fold-thrust belts is self-similar and showed good comparisons to locally averaged profiles of a variety of mountain ranges.

Much of these analyses have either focused on a prescribed taper of the underthrusting plate (Davis *et al.* 1983; Dahlen *et al.* 1984) or assumed isostatic compensation (Ellis *et al.* 1995). However, over smaller length scales of 10s–100s of km, flexure of the underthrusting plate plays an important role in determining the geometry of the resultant deformation (Forsyth 1985; McKenzie & Fairhead 1997), and should therefore be included for a full description of the fold-thrust belt evolution. Many studies have demonstrated that the patterns of gravity anomalies in the forelands of mountain ranges reveal the elastic flexure of the underthrusting plate in response to the load imposed by the mountain range (e.g. Karner & Watts 1983; Lyon-Caen & Molnar 1983; Snyder & Barazangi 1986; Burov *et al.* 1990; Watts *et al.* 1995; Haddad & Watts 1999; Jordan & Watts 2005). These studies have been concerned with using the present-day pattern of gravity anomalies to infer the flexural properties of the lithosphere. More recently, numerical models have been used to consider the growth and evolution of the coupled system of flexure in the underthrusting plate overlain by shortening and thickening to form a fold-thrust belt. In particular, studies have focused on coupling flexure with complex rheologies such as an elasto-visco-plastic wedge (Simpson 2006, 2010; Stockmal *et al.* 2007) and a Coulomb wedge (Wang 2001). However, a simplified model combining wedge deformation with flexure in the underthrusting plate is yet lacking.

In the next section, we build on this previous work by considering the growth of a fold-thrust belt in which the underthrusting plate deforms elastically in response to the evolving overlying fold-thrust belt. We consider a purely viscous rheology to model the long wavelength topography associated with fold-thrust belts on length scales much larger than individual faults (England & McKenzie 1982). This rheology is chosen for its simplicity, and ability to accommodate distributed and spatially variable deformation, and is appropriate if a large proportion of the deformation is by fluid-activated or thermally activated creep mechanisms (Rutter 1983). The low to absent rates of seismicity in the regions to which we apply our model may support this assumption (see next). In Section 5.3, we will compare the results of our viscous model to that of a Coulomb wedge model.

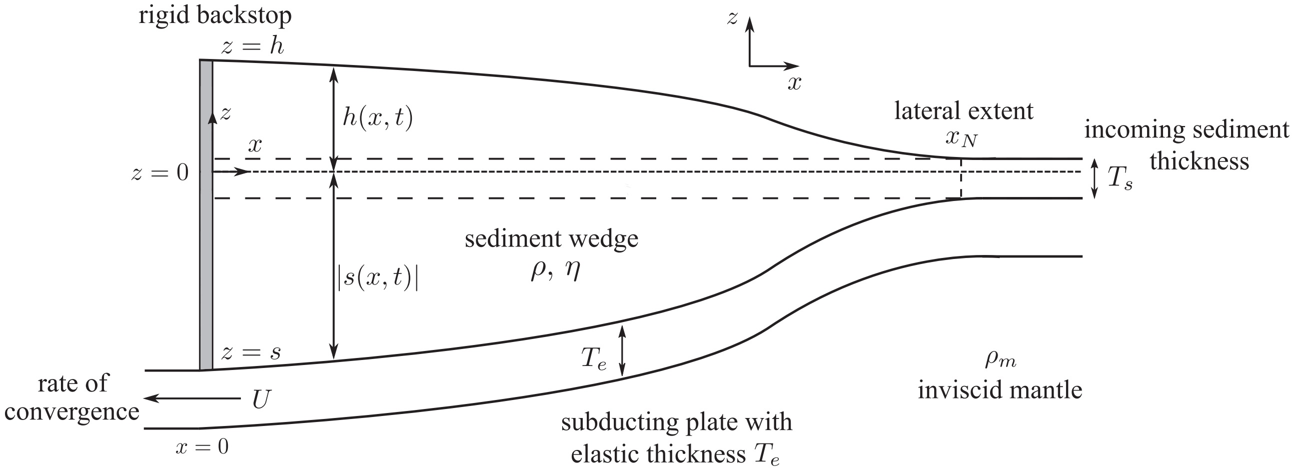

Figure 1. Schematic showing the 2-D theoretical model for the cross-section of a fold-thrust belt with the physical parameters in the system defined as topographic height h, plate deflection s, lateral extent x_N, incoming sediment thickness T_s, sediment and mantle densities ρ and ρ_m, and viscosity η, and underthrusting plate with elastic thickness T_e and convergence velocity U.

3 MODEL SET-UP

We consider a 2-D model of a fold-thrust belt as shown in Fig. 1. Incoming sediment is modelled as a viscous fluid with density ρ, and viscosity η, and the underlying mantle below as an inviscid fluid with density ρ_m. (For a submarine wedge, ρ should be replaced by $\bar{\rho} = \rho - \rho_w$, where ρ_w is the density of water). We take an initial configuration at time $t = 0$ in which the wedge consists of a uniform layer of sediment of thickness T_s. The height $h(x, t)$ is the portion of the wedge above $z = 0$, and $s(x, t)$ is the depth of the interface below $z = 0$, defined as negative in the model. The lateral extent x_N is determined by considering the width of the topography above a threshold value as described in Section 4.4. For distances along the x-axis much greater than x_N, the layer is in isostatic balance with the mantle beyond the nose of the thrust belt (see Fig. 1). The underthrusting plate is modelled as a thin elastic beam translating horizontally with speed U towards the backstop, with elastic thickness T_e, Young's modulus E, Poisson's ratio ν and hence bending stiffness $B = T_e^3 E/12(1 - \nu^2)$. The viscous sediment layer is advected with this plate towards the backstop. We define the convergence velocity U as the total rate of motion between the incoming plate and the backstop. The backstop, which is fixed at $x = 0$, represents a region of overlying plate that is stronger than the incoming sediments. Here, we assume that the backstop remains undeformed during the evolution of the thrust belt and prevents any flow of sediment out of the model domain.

Geological and geophysical observations show that the typical vertical thickness of a thrust belt is much smaller than the across-strike width, therefore, lubrication theory (flow in a thin viscous layer) can be used to model deformation in the wedge (Schlichting & Shapiro 1979). The rate of change of the thickness of the wedge $(h - s)$ due to advection of sediment and strain within the wedge can be written as an advection–diffusion equation (e.g. Perazzo & Gratton 2008):

$$\frac{\partial}{\partial t}(h - s) = \frac{\rho g}{3\eta}\frac{\partial}{\partial x}\left[(h - s)^3 \frac{\partial h}{\partial x}\right] + U\frac{\partial}{\partial x}(h - s). \qquad (1)$$

Across the wedge, there is a balance between the flexural subsidence of the plate due to the mass of the overlying wedge and the hydrostatic restoring force of the underlying mantle as a result of this subsidence. This balance is defined by the Euler–Bernoulli beam equation (Timoshenko & Woinowsky-Krieger 1959):

$$B\frac{\partial^4 s}{\partial x^4} + \rho_m g s = -\rho g(h - s). \qquad (2)$$

We apply boundary conditions by first imposing no flow of sediment through the backstop at $x = 0$:

$$-\frac{\rho g}{3\eta}(h - s)^3 \left.\frac{\partial h}{\partial x}\right|_{x=0} = U\,(h - s)|_{x=0}\,. \qquad (3)$$

We assume that loading behind the backstop does not affect the deformation of the underthrusting plate and therefore impose a mechanical break in the plate at $x = 0$ by setting the bending moment and shear force to be zero:

$$\left.\frac{\partial^2 s}{\partial x^2}\right|_{x=0} = \left.\frac{\partial^3 s}{\partial x^3}\right|_{x=0} = 0, \qquad (4)$$

respectively. We impose a uniform sediment layer thickness in the far field, which is in isostatic balance with the underlying mantle below:

$$h \to h_\infty, \quad s \to s_\infty = -\frac{\rho}{\rho_m - \rho}h_\infty \quad \text{as} \quad x \to \infty, \qquad (5)$$

such that $h_\infty - s_\infty = T_s$ is the far-field sediment layer thickness. Finally, far from the loading in the wedge the underthrusting plate is undeformed so that deflections decay:

$$\frac{\partial s}{\partial x} \to 0 \quad \text{as} \quad x \to \infty. \tag{6}$$

There are several natural length and timescales in the problem, with which we determine a universal, non-dimensional problem. In the horizontal, the length scale at which the weight of the wedge begins to dominate over the strength of the plate is defined as the flexural parameter (also known as the elastogravity length scale), which has units of length

$$l_e = \left(\frac{B}{\Delta\rho g}\right)^{1/4}, \tag{7}$$

where $\Delta\rho = \rho_m - \rho > 0$ is the density difference between the mantle and the sediment in the wedge. By balancing the evolution of the thickness of the wedge with the advection of sediment and strain within the wedge, as described by eq. (1), we may write the characteristic vertical height and timescales as

$$H = \left(\frac{3\eta U l_e}{\rho g}\right)^{1/3}, \quad T = \frac{l_e}{U}. \tag{8}$$

Hence, we can define non-dimensional variables

$$\tilde{h} = \frac{h}{H} \equiv h\left(\frac{\rho g}{3\eta U l_e}\right)^{1/3}, \quad \tilde{x} = \frac{x}{l_e} \quad \text{and} \quad \tilde{t} = \frac{t}{T} \equiv t\frac{U}{l_e}. \tag{9}$$

The non-dimensional equations are, therefore, functions of only two parameters:

$$\lambda = \frac{\rho}{\rho_m - \rho} \equiv \frac{\rho}{\Delta\rho} \quad \text{and} \quad H_\infty = T_s\left(\frac{\rho g}{3\eta U l_e}\right)^{1/3}. \tag{10}$$

The density ratio $\lambda = \rho/\Delta\rho$ describes the proportion of the wedge thickness accommodated by downward deflection of the underthrusting plate in isostatic balance. The parameter H_∞ is the ratio of buoyancy forces to the compressive forces, over the length scale of the flexural parameter. H_∞ is, therefore, equivalent to the Argand number (often expressed as the ratio between the stress from buoyancy to the stress needed to deform the material; England & McKenzie 1982), with the addition of flexural effects.

Dropping the hat decoration, the non-dimensional equations can be written as

$$\frac{\partial}{\partial t}(h - s) = \frac{\partial}{\partial x}\left[(h - s)^3 \frac{\partial h}{\partial x}\right] + \frac{\partial}{\partial x}(h - s), \tag{11}$$

$$\frac{\partial^4 s}{\partial x^4} + s = -\lambda h, \tag{12}$$

with boundary conditions

$$(h - s)^2 \frac{\partial h}{\partial x} = -1, \quad \frac{\partial^2 s}{\partial x^2} = \frac{\partial^3 s}{\partial x^3} = 0 \quad \text{at} \quad x = 0, \tag{13}$$

$$h \to \frac{H_\infty}{1 + \lambda}, \quad s \to -\frac{\lambda H_\infty}{1 + \lambda}, \quad \frac{\partial s}{\partial x} \to 0 \quad \text{as} \quad x \to \infty. \tag{14}$$

The total volume accumulated in the wedge due to advection is given by

$$H_\infty t = \int_0^\infty (h - s - H_\infty)\,\mathrm{d}x. \tag{15}$$

This statement of global mass conservation is a direct consequence of local mass conservation and the requirement of zero flow of sediment through the backstop and out of the model domain, given by eq. (3). By varying λ and H_∞, the full parameter space can be explored for properties of the incoming sediment and underthrusting plate.

In deriving this model, we have made several assumptions in order to reduce the number of unknown parameters. First, we model the underthrusting plate as a thin elastic beam resting on a fluid mantle. We assume that the timescale over which the wedge evolves is much longer than the viscous relaxation time of the underlying mantle, and shorter than that of the lithosphere (Walcott 1970; Watts *et al.* 2013). Second, by modelling the sediment as a viscous fluid we assume that the viscosity of the sediment is much smaller than that of the underthrusting plate (Brace & Kohlstedt 1980). Ellis *et al.* (1995) included the viscosity of the underlying mantle in their analysis when considering crustal thickening at convergent margins, and showed that the coupling to the mantle can be neglected when the wedge is weakly coupled to its base, or when depth of the underlying mantle is large compared with the deflection of the underthrusting plate, as we assume in our model. A basally driven model can then be used, where the underlying mantle is inviscid in comparison to the sedimentary wedge and only provides a hydrostatic restoring force to the wedge.

At the backstop, we impose the boundary condition that there is no flow of sediment out of the wedge. It would be relatively straightforward to include the subduction of deformable sediment in the model (Shreve & Cloos 1986). Doing so would not change the qualitative results of the model but would make the analysis more complex. In our analysis to follow, we refer to the bottom of the wedge as the underthrusting plate but this should be thought of as the base of the deformable sediment, and we treat lithified sediment that is mechanically coupled to the underthrusting plate as part of the plate. In addition, we also neglect any erosion of the topography, which would generally smooth the topographic surface, but again have no impact on the qualitative results described.

Finally, we assume a Newtonian viscous rheology for the sediment in the thrust belt, meaning that the stress is linearly related to the strain rate. Our model can be extended to a power-law rheology. For a power-law rheology, the stress is proportional to some power of the strain rate, allowing effective viscosities to reduce with increased shear stress. We anticipate that, as for a convergent Newtonian viscous gravity current on a horizontal non-deforming base (Gratton & Perazzo 2009), a power-law rheology would give fold-thrust belts with steeper surface gradients and hence imply larger bulk viscosities than the Newtonian equivalent. However, for simplicity, and because diffusion creep results in a Newtonian rheology, we use a Newtonian viscous fluid in our models.

4 MODEL RESULTS

In this section, we describe the different regimes of wedge evolution due to the competition between elastic deformation of the underthrusting plate, advection of sediment and strain within the wedge. We first give a brief overview of the key results and regimes of wedge evolution in Section 4.1. Then, in Sections 4.2 and 4.3, we derive the analytical results underpinning these model regimes along with examples of the shapes and vertical and horizontal length scales of wedges in each regime. Finally, in Section 4.4 we describe the numerical solutions of the fully coupled system to investigate the transition between these regimes.

4.1 Overview of regimes of wedge evolution

The wedge evolves from early to late time depending on the vertical and horizontal length scales. We define ‘early times’ as when the lateral extent of the wedge is much less than the flexural parameter l_e (non-dimensional extent $x_N \ll 1$) and the vertical thickness of the wedge is much less than the incoming non-dimensional sediment height $H_\infty/(1+\lambda) = T_s(\rho g/3\eta U l_e)^{1/3}/(1+\lambda)$, where the density ratio $\lambda = \rho/\Delta\rho$. We define ‘late times’ as when the lateral extent of the wedge is much greater than the flexural parameter (non-dimensional extent $x_N \gg 1$) and the vertical thickness of the wedge is much greater than the incoming non-dimensional sediment height $H_\infty/(1+\lambda)$. By balancing the sediment flux due to strain within the wedge with the flux due to advection of sediment on the underthrusting plate, we define a critical non-dimensional parameter $\Lambda_C = \pi^{1/2}H_\infty^3/(1+\lambda)$. The evolution of the wedge from early to late time depends on the value of this parameter, and describes whether lateral spreading due to strain within the wedge or vertical thickening due to advection of sediment is the dominant mechanism for growth. From now on, we will refer to lateral spreading due to strain within the wedge as ‘gravitational spreading’, where the lateral extent increases due to gravity acting on topography. For a wedge with a low viscosity, high density and thick incoming sediment layer, and an underthrusting plate with a small elastic thickness and convergence velocity (i.e. large critical non-dimensional parameter $\Lambda_C \gg 1$), the initial evolution is predominantly through gravitational spreading, with little vertical thickening due to advection of sediment. In contrast, for a wedge with a high viscosity, low density and thin incoming sediment layer, and an underthrusting plate with a large elastic thickness and convergence velocity (i.e. small $\Lambda_C \ll 1$), the initial evolution is predominantly through vertical thickening due to advection of sediment, with little gravitational spreading.

Fig. 2 plots the lateral extent of the wedge x_N against the normalized maximum topographic height at the backstop, $h_0 = h(0, t)$. The points are calculated numerically as described next in Section 4.4, where different symbols represent different values of the non-dimensional parameters H_∞ and λ, and hence Λ_C, with increasing time going from the bottom left to the top right of the graph. Fig. 2 is split into four quadrants, as shown by the vertical and horizontal dashed lines, to indicate the four regimes: early time; intermediate time, gravitational spreading dominant; intermediate time, vertical thickening dominant and late time. The schematics (i)–(iv) in Fig. 2 demonstrate the key scalings for the vertical and horizontal length scales of the wedge for these regimes from the theoretical analysis described next. The early- and late-time regimes occur in the bottom left-hand and top right-hand quadrants, with scalings represented by schematics (i) and (iv), respectively. When Λ_C is large ($\Lambda_C \gg 1$), the wedge grows predominantly by gravitational spreading, hereafter referred to as Path 1. Evolving through this intermediate regime, the numerical solution passes through the bottom right-hand quadrant with scalings represented by schematic Fig. 2(ii). However, when the parameter Λ_C is small ($\Lambda_C \ll 1$) the wedge grows predominantly by vertical thickening due to advection of sediment, referred to as Path 2. Evolving through this intermediate regime, the numerical solution passes through the top left-hand quadrant with scalings represented by schematic Fig. 2(iii). We will now describe the analytical results underpinning these model regimes along with examples of the size of wedges in each regime.

4.2 Flexural subsidence of the underthrusting plate

The deformation of the underthrusting plate due to the mass of the overlying wedge is dependent on the lateral extent of the sediment load. For small lateral extents, where the sediment has not spread to lengths greater than the flexural parameter l_e (non-dimensional extent $x_N \ll$

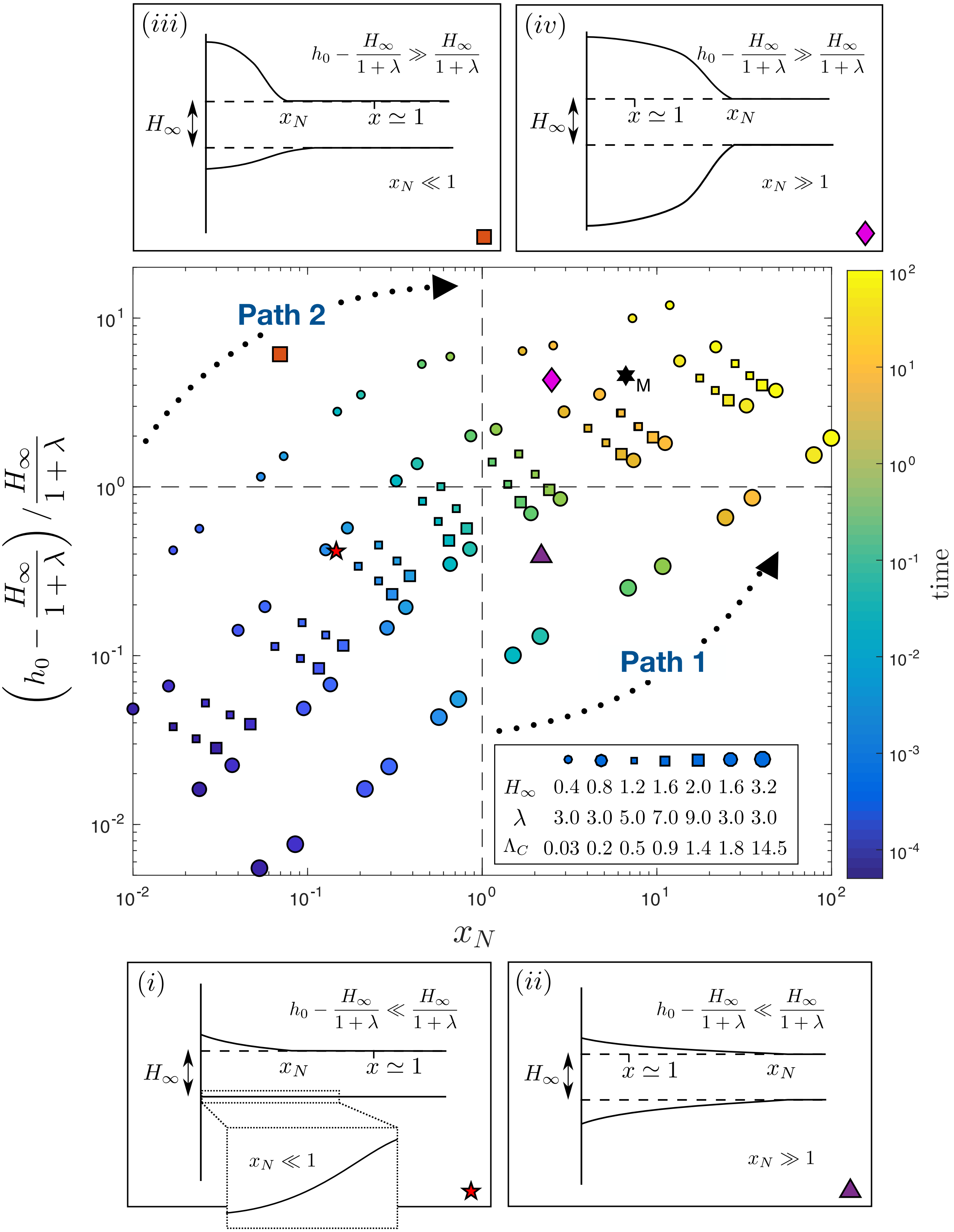

Figure 2. Regime plot. Graph of horizontal extent x_N plotted against maximum vertical topographic height h_0 normalized by the sediment thickness above $z = 0$, $H_\infty/(1 + \lambda)$, for seven different numerical simulations for different values of parameters H_∞ and λ, and hence Λ_C, see legend. Schematics of different regimes of propagation: (i) early-time regime; (ii) intermediate regime along Path 1, where gravitational spreading dominates; (iii) intermediate regime along Path 2, where vertical thickening due to advection of sediment dominates and (iv) late-time regime. The red star, the purple triangle, the orange square and the pink diamond refer to specific examples of wedges in each regime as described in Section 4.3. The black hexagram labelled 'M' refers to the Makran accretionary prism, see Section 5.1.

1), the loading due to the wedge can be approximated as a point force localized at the position of the backstop $x = 0$. Assuming also that the increase in the thickness of sediment is small compared with the total incoming sediment thickness, $(h - s) - H_\infty \ll H_\infty$, eq. (12), describing the flexural subsidence of the plate, reduces to

$$\frac{\partial^4 s}{\partial x^4} + (1+\lambda)s \simeq -\lambda H_\infty. \tag{16}$$

Boundary conditions at the backstop and in the far field can now be applied (eqs 13 and 14) with the condition of zero shear force being replaced by the approximation of a point loading force:

$$\left.\frac{\partial^3 s}{\partial x^3}\right|_{x=0} = -\lambda H_\infty t. \tag{17}$$

Hence, the deflection of the underthrusting plate for $x_\mathrm{N} \ll 1$ is given by

$$s = -\frac{\lambda H_\infty}{1+\lambda}\left[1 + \sqrt{2}(1+\lambda)^{1/4} t e^{-mx} \cos mx\right], \tag{18}$$

where $m = (1+\lambda)^{1/4}/\sqrt{2}$. The maximum deflection is $\sqrt{2}\lambda H_\infty t/(1+\lambda)^{3/4}$ with oscillations that decay to the far-field deflection $-\lambda H_\infty/(1 + \lambda)$, with decay rate and wavelength $1/m$.

When the lateral extent of the sediment load is much greater than the flexural parameter ($x_\mathrm{N} \gg 1$), the underthrusting plate can no longer support the topography. The pressure due to the deflection of the plate is now dominated by a balance between the loading of the wedge and the hydrostatic restoring force of the underlying mantle. For large lateral extents, the wedge, therefore, transitions into isostatic balance where

$$s(x, t) = -\lambda h(x, t), \tag{19}$$

except near the nose region, where flexure of the plate remains important on length scales comparable to the flexural parameter.

4.3 Height of topography

4.3.1 *Early time*

The evolution of the height of the wedge h depends on the relative height of the wedge compared with incoming non-dimensional sediment height $H_\infty/(1 + \lambda)$ above $z = 0$. Initially, the height of the wedge is small compared with the height of the advected sediment layer, $h_0 - H_\infty/(1 + \lambda) \ll H_\infty/(1 + \lambda)$. In addition, the added load of the wedge is insufficient to significantly deform the plate and hence the underthrusting plate remains undeformed with $s \simeq -\lambda H_\infty/(1 + \lambda)$. We can, therefore, linearize the governing equation for the height of the wedge above the far-field sediment height. A scaling of eq. (11) suggests that initially thickening due to advection is small:

$$\frac{h}{t} \sim \frac{H_\infty^3 h}{x^2} \gg \frac{h}{x} \quad \text{provided} \quad x_N \ll H_\infty^3, \tag{20}$$

giving height and extent scales $h - H_\infty/(1 + \lambda) \sim H_\infty^{-1/2} t^{1/2}$ and $x_N \sim H_\infty^{3/2} t^{1/2}$, respectively. In this limit, the topography of the wedge is self-similar. Therefore, we may define the similarity variable $\zeta = x/(4H_\infty^3 t)^{1/2}$ and write $h = H_\infty/(1 + \lambda) + t^{1/2} f(\zeta),\ s \simeq -\lambda H_\infty/(1 + \lambda)$, where f is a solution to the nonlinear ordinary differential equation:

$$\frac{\partial^2 f}{\partial \zeta^2} + 2\zeta\frac{\partial f}{\partial \zeta} - 2f = 0 \quad \Rightarrow \quad f = c_1\zeta + c_2\left[\pi^{1/2}\zeta\,\mathrm{erfc}(\zeta) - \exp(-\zeta^2)\right], \tag{21}$$

and c_1, c_2 are constants of integration that need to be determined by applying boundary conditions at the backstop and in the far field. Linearizing the boundary conditions (eqs 13 and 14),

$$H_\infty^2 \left.\frac{\partial h}{\partial x}\right|_{x=0} = -1 \quad \text{and} \quad h(x \to \infty) \to \frac{H_\infty}{1+\lambda}, \tag{22}$$

and applying these to the general solution for f (eq. 21), then gives an expression for the topographic height of an accretionary wedge in the early-time regime:

$$h = \frac{H_\infty}{1+\lambda} + \frac{2t^{1/2}}{(\pi H_\infty)^{1/2}}\left[\exp\left(-\frac{x^2}{4H_\infty^3 t}\right) - \frac{\pi^{1/2}x}{2(H_\infty^3 t)^{1/2}}\,\mathrm{erfc}\left(\frac{x}{2(H_\infty^3 t)^{1/2}}\right)\right]. \tag{23}$$

This analytical result is shown by Perazzo & Gratton (2008) for a viscous convergent gravity current on a horizontal, non-deformable base. The maximum topographic height is $H_\infty/(1 + \lambda) + 2t^{1/2}/(\pi H_\infty)^{1/2}$, which decays monotonically to the far-field sediment layer height $H_\infty/(1 + \lambda)$, with lateral extent given by $x_\mathrm{N} \sim 2H_\infty^{3/2} t^{1/2}$. Eq. (23) for the topographic height along with eq. (18) for the deflection of the underlying plate defines the early-time regime where lateral extent of the wedge is much less than the flexural parameter l_e and the vertical height is much less than the non-dimensional incoming sediment height $H_\infty/(1 + \lambda)$. Applying these bounds ($x_\mathrm{N} \ll 1$ and $h_0 - H_\infty/(1 + \lambda) \ll H_\infty/(1$

$+ \lambda)$) to the scalings from eq. (23) gives a timescale for the early-time regime:

$$2H_\infty^{3/2} t^{1/2} \ll 1 \quad \text{and} \quad \frac{2t^{1/2}}{(\pi H_\infty)^{1/2}} \ll \frac{H_\infty}{1+\lambda} \quad \Rightarrow \quad t \ll \min\left\{\frac{\pi H_\infty^3}{4(1+\lambda)^2}, \frac{1}{4H_\infty^3}\right\}. \tag{24}$$

To indicate when the early-time regime may be appropriate in nature, we consider a wedge with common values of parameters of sediment thickness, viscosity and density $T_s = 4\,\text{km}$, $\eta = 10^{20}\,\text{Pa s}$ and $\rho = 2400\,\text{kg m}^{-3}$, respectively, where the underthrusting plate has an elastic thickness of $T_e = 20\,\text{km}$, Young's modulus $E = 10^{11}\,\text{Pa}$, Poisson's ratio $\nu = 0.25$ and convergence velocity $U = 4\,\text{mm yr}^{-1}$, with an underlying mantle of density $\rho_m = 3300\,\text{kg m}^{-3}$ ($H_\infty = 0.91,\ \lambda = 2.7$). For an age of $t = 0.1$ Myr, this gives a maximum topographic height of ~450 m above the far-field sediment height, with lateral extent of ~8 km. From eq. (18), the maximum deflection of the plate is ~43 m with decay rate and wavelength ~54 km. Substituting these parameters into timescale given in eq. (24) shows that the conditions for early-time regime behaviour are satisfied provided $t \ll 1$ Myr. Hence, these behaviours are not expected to be observed except in the very early stages of wedge growth. In Fig. 2, this early-time regime represents the bottom left-hand quadrant where $x_N \ll 1$ and $h_0 - H_\infty/(1 + \lambda) \ll H_\infty/(1 + \lambda)$. This example is marked as a red star in the bottom left-hand quadrant of Fig. 2, and is demonstrated by the schematic (i).

4.3.2 *Intermediate time: gravitational spreading dominant*

After this early-time regime, the wedge can either grow by gravitational spreading or vertical thickening. If the wedge spreads laterally more rapidly than it thickens vertically, referred to as Path 1 (Fig. 2), it can reach an intermediate regime where the lateral extent of the wedge is much greater than the flexural parameter l_e but the vertical height of the wedge is still much less than the non-dimensional sediment height $H_\infty/(1 + \lambda)$. Applying these bounds ($x_N \gg 1$ and $h_0 - H_\infty/(1 + \lambda) \ll H_\infty/(1 + \lambda)$) to the solution for the early-time topographic height, eq. (23) gives a condition for evolution along Path 1:

$$2H_\infty^{3/2} t^{1/2} \sim 1 \quad \text{and} \quad \frac{2t^{1/2}}{(\pi H_\infty)^{1/2}} \ll \frac{H_\infty}{1+\lambda} \quad \Rightarrow \quad \Lambda_C \equiv \frac{\pi^{1/2} H_\infty^3}{1+\lambda} \gg 1, \tag{25}$$

where Λ_C is the critical non-dimensional parameter defined above, the effect of which is described next.

Since the lateral extent of the wedge is much greater than the flexural parameter ($x_N \gg 1$), the wedge is in isostatic balance and the deflection of the plate is linearly proportional to the topographic height, given by eq. (19). Substituting this expression for the deflection s into eq. (11), and carrying out a similar analysis to above, gives an expression for the topography of a wedge in the intermediate regime evolving along Path 1:

$$h = \frac{H_\infty}{1+\lambda} + \frac{2t^{1/2}}{(\pi(1+\lambda)H_\infty)^{1/2}}\left[\exp\left(-\frac{(1+\lambda)x^2}{4H_\infty^3 t}\right) - \frac{(\pi(1+\lambda))^{1/2}x}{2(H_\infty^3 t)^{1/2}}\,\text{erfc}\left(\frac{(1+\lambda)^{1/2}x}{2(H_\infty^3 t)^{1/2}}\right)\right]. \tag{26}$$

The maximum topographic height is $H_\infty/(1 + \lambda) + 2t^{1/2}/(\pi(1 + \lambda)H_\infty)^{1/2}$, which decays monotonically to the far-field sediment layer height $H_\infty/(1 + \lambda)$, with lateral extent given by $x_N \sim 2H_\infty^{3/2} t^{1/2}/(1 + \lambda)^{1/2}$. To demonstrate evolution of a wedge along Path 1, we consider a wedge with sediment thickness, viscosity and density $T_s = 10\,\text{km}$, $\eta = 10^{20}\,\text{Pa s}$ and $\rho = 2400\,\text{kg m}^{-3}$, respectively, where the underthrusting plate has an elastic thickness of $T_e = 20\,\text{km}$, Young's modulus $E = 10^{11}\,\text{Pa}$, Poisson's ratio $\nu = 0.25$ and convergence velocity $U = 4\text{mm yr}^{-1}$, with an underlying mantle of density $\rho_m = 3300\,\text{kg m}^{-3}$ ($H_\infty = 2.3,\ \lambda = 2.7$). Substituting these values into eq. (25) gives critical non-dimensional parameter $\Lambda_C = 5.6 \gg 1$, hence we would expect the wedge to evolve along Path 1. Taking a wedge of age $t = 5$ Myr gives a maximum topographic height of ~1.1 km above the far-field sediment height, maximum deflection of the plate of ~2.8 km and a lateral extent of ~120 km. In Fig. 2, this intermediate regime evolving along Path 1 represents the bottom right-hand quadrant where $x_N \gg 1$ and $h_0 - H_\infty/(1 + \lambda) \ll H_\infty/(1 + \lambda)$. This example is marked as a purple triangle in the bottom right-hand quadrant of Fig. 2, and is demonstrated by the schematic (ii). This evolution represents regions where the incoming sediment layer is thick with low viscosity and high density, and the underthrusting plate has a small elastic thickness and small convergence velocity.

4.3.3 *Intermediate time: thickening dominant*

If the wedge thickens vertically more rapidly than it spreads laterally, it follows an alternative evolution referred to as Path 2. Along this second trajectory, the wedge can reach an intermediate regime where the lateral extent of the wedge is still much less than the flexural parameter but the vertical height of the wedge is much greater than the non-dimensional sediment height $H_\infty/(1 + \lambda)$. Applying these bounds ($x_N \ll 1$ and $h_0 - H_\infty/(1 + \lambda) \gg H_\infty/(1 + \lambda)$) to the solution for the early-time topographic height, eq. (23), gives a condition for evolution along Path 2:

$$2H_\infty^{3/2} t^{1/2} \ll 1 \quad \text{and} \quad \frac{2t^{1/2}}{(\pi H_\infty)^{1/2}} \sim \frac{H_\infty}{1+\lambda} \quad \Rightarrow \quad \Lambda_C \equiv \frac{\pi^{1/2} H_\infty^3}{1+\lambda} \ll 1. \tag{27}$$

Since the vertical height of the wedge is much greater than the non-dimensional incoming sediment height $H_\infty/(1 + \lambda)$, the height of the wedge reaches a quasi-static balance where strain driven by lateral pressure gradients, which results in gravitational slumping and hence diffusive behaviour, balances the advection of the sediment layer by the underthrusting plate. The governing equation for the thickness of the wedge (eq. 11) simplifies to

$$0 = \frac{\partial}{\partial x}\left[(h-s)^3\frac{\partial h}{\partial x}\right] + \frac{\partial}{\partial x}(h-s). \tag{28}$$

Integrating eq. (28), assuming the underthrusting plate remains relatively undeformed $s \simeq -\lambda H_\infty/(1+\lambda)$, and applying boundary conditions at the backstop and at the nose (eqs 13 and 14), gives the expression for the topographic height

$$h = -\frac{\lambda H_\infty}{1+\lambda} + \left[H_\infty^3 + 3(x_N - x)\right]^{1/3}. \tag{29}$$

Using the statement of global conservation of mass (eq. 15), we find that the lateral extent x_{N} is the real root of

$$H_\infty\left(\frac{1}{4}H_\infty^3 + x_N + t\right) = \frac{1}{4}(H_\infty^3 + 3x_N)^{4/3}. \tag{30}$$

Eq. (29) describes a cube root profile, where the topographic height no longer explicitly depends on time (although there is an implicit time dependence through the lateral extent x_{N}), and hence can be described as quasi-static. For example, consider a wedge with sediment thickness, viscosity and density $T_{\mathrm{s}} = 1\,\mathrm{km}$, $\eta = 10^{20}\,\mathrm{Pa\,s}$ and $\rho = 2400\,\mathrm{kg\,m^{-3}}$, respectively, where the underthrusting plate has an elastic thickness of $T_{\mathrm{e}} = 20\,\mathrm{km}$, Young's modulus $E = 10^{11}\,\mathrm{Pa}$, Poisson's ratio $\nu = 0.25$ and convergence velocity $U = 4\,\mathrm{mm\,yr^{-1}}$, with an underlying mantle of density $\rho_{\mathrm{m}} = 3300\,\mathrm{kg\,m^{-3}}$ ($H_\infty = 0.23$, $\lambda = 2.7$). Substituting these values into eq. (27) gives critical non-dimensional parameter $\Lambda_{\mathrm{C}} = 0.0056 \ll 1$, hence we would expect the wedge to evolve along Path 2. Taking a wedge of age $t = 1$ Myr gives a maximum topographic height of ~1.7 km above the far-field sediment height, with lateral extent ~3.7 km. From eq. (18), the maximum deflection of the plate is ~110 m with decay rate and wavelength ~54 km. In Fig. 2, this intermediate regime evolving along Path 2 represents the top left-hand quadrant, where $x_{\mathrm{N}} \ll 1$ and $h_0 - H_\infty/(1+\lambda) \gg H_\infty/(1+\lambda)$. This example is marked as an orange square in the top left-hand quadrant of Fig. 2, and is demonstrated by the schematic (iii). This path represents regions where the incoming sediment layer is thin with a high viscosity and low density, and the underthrusting plate has a large elastic thickness and a high convergence rate.

4.3.4 Late time

Ultimately, the evolution of a wedge along both Path 1 or Path 2 will transition into the late-time regime where the lateral extent of the wedge is much greater than the flexural parameter ($x_{\mathrm{N}} \gg 1$) and the height of the wedge is much greater than the non-dimensional sediment height ($h_0 - H_\infty/(1+\lambda) \gg H_\infty/(1+\lambda)$). Since the lateral extent is much greater than the flexural parameter ($x_{\mathrm{N}} \gg 1$), the wedge is in isostatic balance with deflection given by eq. (19). As in the intermediate regime along Path 2, the wedge is in a quasi-static state where strain balances the advection of the sediment layer by the underthrusting plate. Substituting the deflection (eq. 19) into the governing equation for the quasi-static wedge (eq. 28), integrating and applying boundary conditions at the backstop and the nose (eqs 13 and 14), the topographic height is given by

$$h = \left[\frac{H_\infty^3}{(1+\lambda)^3} + \frac{3(x_N - x)}{(1+\lambda)^2}\right]^{1/3}. \tag{31}$$

Again, using the statement of global conservation of mass (eq. 15), we find that the lateral extent x_{N} is the real root of

$$H_\infty\left(\frac{H_\infty^3}{4(1+\lambda)} + x_{\mathrm{N}} + t\right) = \frac{1}{4(1+\lambda)}(H_\infty^3 + 3(1+\lambda)x_{\mathrm{N}})^{4/3}. \tag{32}$$

Eq. (31) describes a cube root profile where the topographic height of the wedge no longer explicitly depends on time (although there is an implicit time dependence through the lateral extent x_{N}). For example, consider a wedge with sediment thickness, viscosity and density $T_{\mathrm{s}} = 2\,\mathrm{km}$, $\eta = 10^{19}\,\mathrm{Pa\,s}$, $\rho = 2400\,\mathrm{kg\,m^{-3}}$, respectively, where the underthrusting plate has an elastic thickness of $T_{\mathrm{e}} = 20\,\mathrm{km}$, Young's modulus $E = 10^{11}\,\mathrm{Pa}$, Poisson's ratio $\nu = 0.25$ and convergence velocity $U = 20\,\mathrm{mm\,yr^{-1}}$, with an underlying mantle of density $\rho_{\mathrm{m}} = 3300\,\mathrm{kg\,m^{-3}}$ ($H_\infty = 0.57$, $\lambda = 2.7$). For an age of $t = 20$ Myr, the wedge would have a maximum topographic height ~2.3 km above the far-field height, maximum deflection of the plate of ~6.3 km, with lateral extent ~130 km. In Fig. 2, this late-time regime represents the top right-hand quadrant, where $x_{\mathrm{N}} \gg 1$ and $h_0 - H_\infty/(1+\lambda) \gg H_\infty/(1+\lambda)$. This example is marked as a pink diamond in the top right-hand quadrant of Fig. 2, and is demonstrated by the schematic (iv).

The analytical solutions derived above describe the limiting case in each of the four regimes shown in Fig. 2. However, a given fold-thrust belt will lie along an evolutionary transition between these solutions. In order to fully understand how a fold-thrust belt evolves, in the next section we solve this coupled system numerically. In particular, we describe the full evolution of two wedges, one evolving along Path 1, and one evolving along Path 2.

4.4 Numerical solutions

We solve the coupled system of non-dimensional equations for the evolution of the topographic height and the flexural subsidence of the underthrusting plate given by eqs (11) and (12) along with boundary conditions at the backstop and in the far field (eqs 13 and 14), and global mass conservation (eq. 15). The numerical scheme uses a finite difference Crank–Nicolson algorithm with an adaptive time and spatial step, and a predictor–corrector scheme to handle the nonlinearities.

Fig. 2 plots the vertical topographic height against the lateral extent for seven different numerical simulations with different values of non-dimensional parameters H_∞ and λ (see legend inset). Note that the location of the lateral extent x_N is determined by considering the width of topography above a threshold value such that $h(x_N, t) - H_\infty/(1+\lambda) = 10^{-3}$ at the edge of the wedge, consistent in all simulations. The transition between evolution along Path 1 or Path 2 depends on the critical non-dimensional parameter $\Lambda_C = \pi^{1/2} H_\infty^3/(1+\lambda)$. Fig. 2 shows that by decreasing Λ_C the evolution moves from Path 1 to Path 2 with the transition occurring when $\Lambda_C \sim 1$. In dimensional form, the transition occurs when $\Lambda_C = \pi^{1/2} T_s^3 \rho g/(3\eta U l_e(1+\rho/\Delta\rho)) \sim 1$. Hence, by decreasing the sediment thickness and density and/or increasing the sediment viscosity and elastic thickness and convergence velocity of the underthrusting plate, evolution moves from predominantly gravitational spreading along Path 1 to predominantly vertical thickening along Path 2.

We now describe in more detail the two numerical simulations with the largest and smallest values of Λ_C. Fig. 3(a) plots the profiles of the topographic height (the blue lines) and plate deflection (the red lines) with parameters $H_\infty = 3.2$, $\lambda = 3.0$ and $\Lambda_C = 14.5 \gg 1$ for times $t = 5 \times 10^{-4}, 10^{-3}, \ldots, 10^2$, where Fig. 3(b, inset) is a zoom of profiles at early times ($t \leq 10^{-1}$). Evolution of the wedge is along Path 1, where gravitational spreading dominates over vertical thickening. Fig. 3(c) is a log–log plot of the maximum topographic height (the blue squares) and maximum plate deflection (the red triangles) against time. The dotted and dashed lines plot the early- and late-time solutions, respectively, for the maximum topographic height (blue; eqs 23 and 31) and the maximum plate deflection (red; eqs 18 and 19) and show good agreement with the numerical solution for small and large times. The green dashed line plots the solution between the early and late times for the height of the topographic wedge, defined as the intermediate solution, for evolution along Path 1 (eq. 26). Although it does well to describe the points around $t \sim 1$, the intermediate solution largely overlaps the early-time and late-time solutions and hence does not provide any further information about the growth of the wedge. However, we would anticipate this solution to be more useful (i.e. describe the evolution when both the early and late time do not apply) when there is a larger separation between the early and late time, that is, for larger Λ_C. This evolution describes a wedge with a thick incoming sediment layer of large density and small viscosity, and an underthrusting plate with a small elastic thickness and low convergence velocity.

Fig. 3(d) plots the profiles of the topographic height (the blue lines) and plate deflection (the red lines) with parameters $H_\infty = 0.4$, $\lambda = 3.0$ and $\Lambda_C = 0.03 \ll 1$ for times $t = 5 \times 10^{-4}, 10^{-3}, \ldots, 10^2$, where Fig. 3(e, inset) is a zoom of profiles at early times ($t \leq 1$). Evolution of the wedge is along Path 2, where vertical thickening dominates over gravitational spreading. Fig. 3(f) is a log–log plot of the maximum topographic height (the blue squares) and maximum plate deflection (the red triangles) against time. The dotted and dashed lines plot the early- and late-time solutions, respectively, for the maximum topographic height (blue; eqs 23 and 31) and the maximum plate deflection (red; eqs 18 and 19) and again shows good agreement with the numerical solution for small and large times. The green dashed line plots the solution between early and late times for the height of the topographic wedge (the intermediate solution) for the evolution along Path 2 (eq. 29). This intermediate solution does well to describe the points around $t \sim 1$ where both the early-time and late-time solution do not apply: the numerical solution given by the blue squares sits in between the blue dot–dashed and dashed lines for the early- and late-time solutions, respectively, but sits very close the green dashed line of the intermediate solution. This evolution describes a wedge with a thin incoming sediment layer of small density and large viscosity, and an underthrusting plate with a large elastic thickness and high convergence velocity. Comparing the profiles of the two wedges (Figs 3a and d), there is a clear difference in the nose region of the wedge where there is a prominent flexural depression and bulge when $\Lambda_C = 0.03 \ll 1$ compared with when $\Lambda_C = 14.5 \gg 1$. This forms at early times, Fig. 3(e), and then propagates as a steady structure at the nose, Fig. 3(d). This flexural depression and bulge demonstrates that, even at late times when the wedge is in isostatic balance, flexure remains important on length scales comparable with the flexural parameter l_e. Away from the nose, the general shape of the profiles look similar, however, the underlying balance of forces changes significantly between the two regimes, from gravitational spreading dominant to advection dominant, which is what defines the 'regimes'.

5 DISCUSSION AND APPLICATIONS

The model described above considers how changing the properties of the wedge (density, viscosity, age, incoming sediment thickness) and properties of the underthrusting plate (elastic thickness, convergence velocity) affect the evolution of the wedge. We now discuss the effects of changing two key parameters: the incoming sediment thickness T_s and elastic thickness T_e.

Fig. 4 shows the evolution of a wedge in 5 Myr intervals for $t = 5$–50 Myr, convergence velocity $U = 4\,\mathrm{mm\,yr^{-1}}$, viscosity $\eta = 10^{20}$ Pa s, sediment and underlying mantle densities $\rho = 2400\,\mathrm{kg\,m^{-3}}$, $\rho_m = 3300\,\mathrm{kg\,m^{-3}}$ (density ratio $\lambda = 2.7$). Figs 4(a)–(c) show a wedge in isostatic balance for which we neglect the elastic thickness of the plate ($T_e = 0$ km) with increasing sediment thicknesses $T_s = 2$, 4 and 10 km. Figs 4(d)–(f) show the evolution of an identical series of wedges now resting on a underthrusting plate with an increased elastic thickness of $T_e = 20$ km (Young's Modulus $E = 10^{11}$ Pa and Poisson's ratio $\nu = 0.25$). Substituting these values into the critical non-dimensional parameter Λ_C gives $\Lambda_C = 0.045$, 0.36 and 5.6 for corresponding incoming sediment thicknesses $T_s = 2$, 4 and 10 km. Hence, both Fig. 4 and the values of Λ_C demonstrate that, as described in the previous section, decreasing the incoming sediment thickness causes the evolution to transition from Path 1 (Fig. 4f), to Path 2 (Fig. 4d; decreasing Λ_C), where vertical thickening dominates over gravitational spreading.

For the smallest sediment thickness, $T_s = 2$ km in Figs 4(a) and (d), increasing the elastic thickness gives profiles with a higher maximum topographic elevation for small lateral extents. This is consistent with a stronger plate providing additional support to topography. In addition,

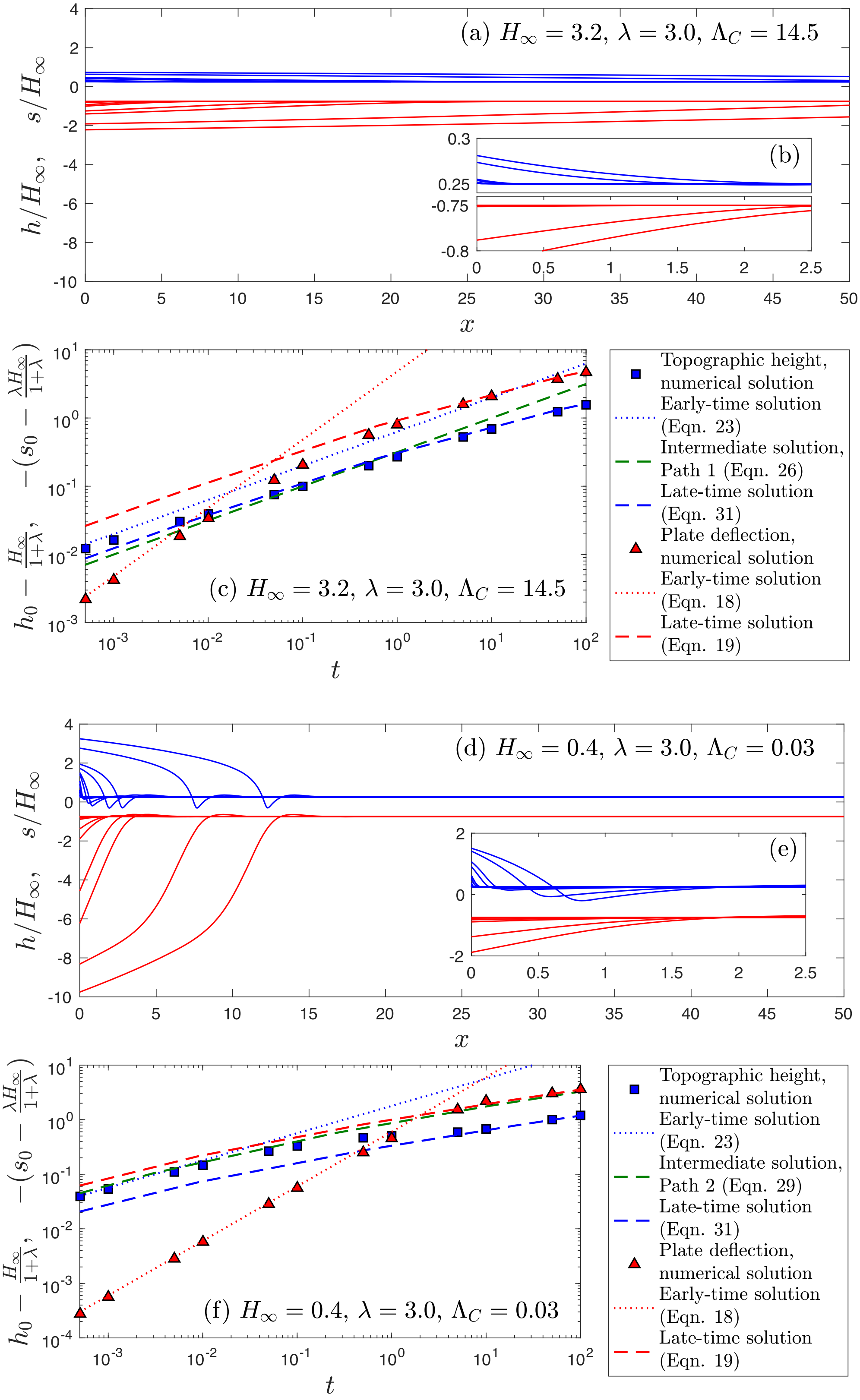

Figure 3. (a) Plot of profiles of the topographic height (the blue lines) and plate deflection (the red lines) for a wedge evolving along Path 1 with parameters $H_\infty = 3.2,\ \lambda = 3.0,\ \Lambda_\mathrm{C} = 14.5$ for $t = 5 \times 10^{-4},\ 10^{-3} \ldots 10^{2}$, where (b, inset) is a zoom in of profiles at early times for $t \leq 10^{-1}$. (c) Log–log plot of the maximum topographic height h_0 (the blue squares) and maximum plate deflection s_0 (the red triangles) against time for each profile shown in (a–b). The dotted and dashed lines plot the early- and late-time solutions, respectively, for the maximum topographic height (blue) and the maximum plate deflection (red). The intermediate solution is given by the green dashed line. See legend for more details. (d–f) Same as (a–c) but for evolution along Path 2 with parameters $H_\infty = 0.4,\ \lambda = 3.0,\ \Lambda_\mathrm{C} = 0.03$, where (e, inset) is a zoom in of profiles at early times for $t \leq 1$.

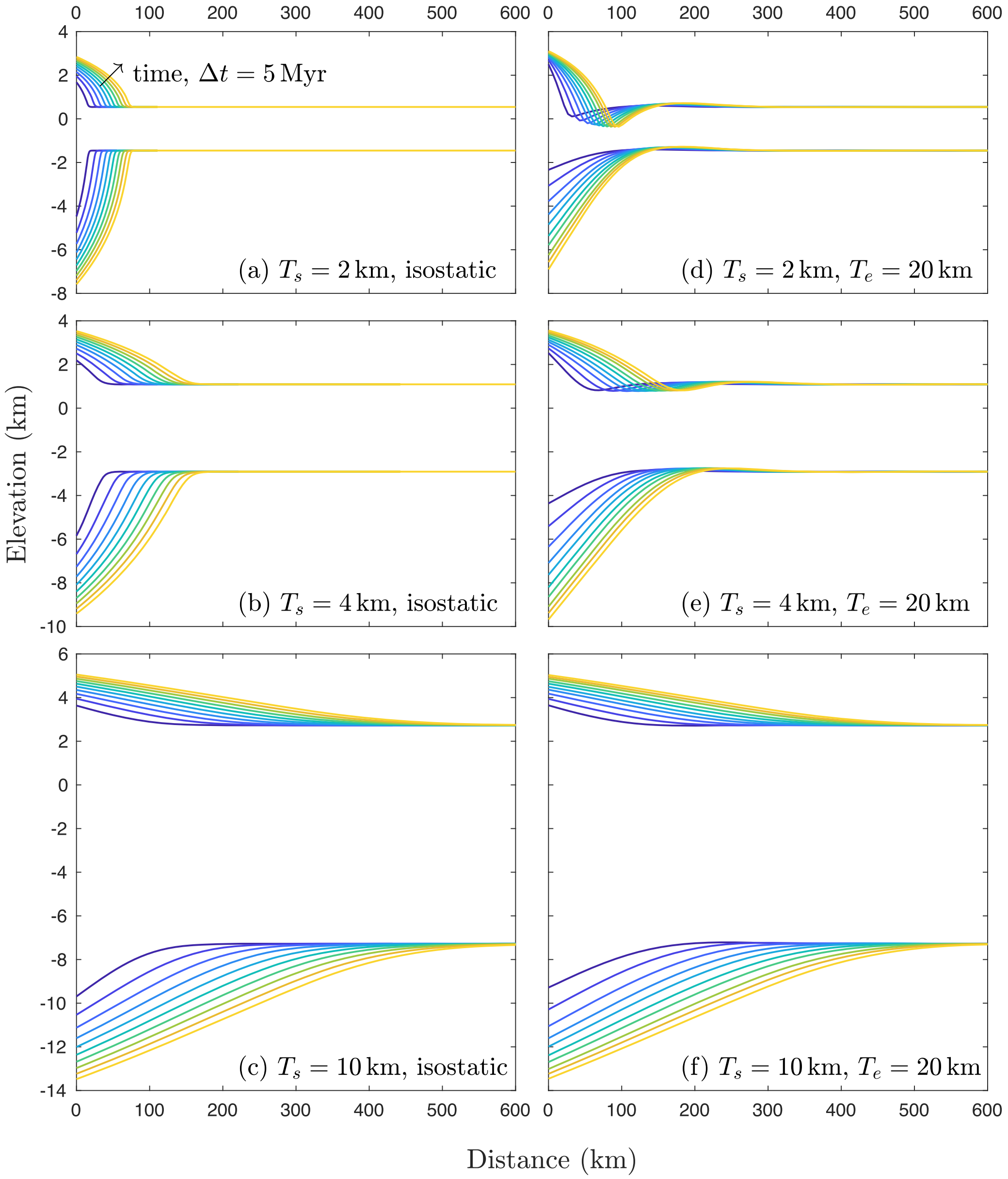

Figure 4. Dimensional plot of the growth of a fold-thrust belt considering the effects of increasing sediment thickness T_s and elastic thickness T_e. (a–c) Evolution of a wedge for $t = 5$–50 Myr and sediment thicknesses $T_s = 2,\ 4,\ 10$ km, respectively, in isostatic balance with no elastic thickness ($T_e = 0$ km). (d–f) Evolution of a wedge with the same sediment thicknesses as plots (a–c) but with elastic thickness $T_e = 20$ km (Young's modulus $E = 10^{11}$ Pa, Poisson's ratio $\nu = 0.25$). In both cases, all other parameters remain the same with convergence velocity $U = 4\,\mathrm{mm\,yr^{-1}}$, viscosity $\eta = 10^{20}$ Pa s, sediment and underlying mantle densities $\rho = 2400\,\mathrm{kg\,m^{-3}},\ \rho_m = 3300\,\mathrm{kg\,m^{-3}}$.

increasing the elastic thickness gives a shallower dip to the deflection of the underthrusting plate behind the nose of the wedge, with a flexural depression and bulge in front of the nose of the wedge, see Figs 4(d) and (e). This feature is present because flexure becomes important when topography varies on length scales comparable with the flexural parameter l_e, for example, near the nose. As the incoming sediment thickness increases, the elastic thickness of the plate has less of an impact on the profiles. This effect is clearly shown in Figs 4(c) and (f) for $T_s = 10$ km, where the profiles of the wedge for the isostatic and flexural case are almost identical. By increasing the incoming sediment thickness, the critical non-dimensional parameter Λ_C increases causing the transition to isostatic balance to occur at earlier times. Hence, we would expect that changing the elastic thickness would have less of an impact for wedges with larger sediment thicknesses.

In order to examine the effects described in our model, we now consider the Makran accretionary prism and the Indo–Burman Ranges. In the analysis, we will refer to specific values of the incoming sediment thickness, viscosity and density, and the elastic properties and convergence velocity of the underthrusting plate. However, the aim is to illustrate the importance of flexure and incoming sediment thickness on the evolution of fold-thrust belts in general, rather than to imply these ranges are particularly unusual.

5.1 Makran accretionary prism

The Makran accretionary prism, Fig. 5(a), is one of the largest accretionary wedges on the Earth. With a large sediment thickness on the incoming plate of ∼7 km (White 1982; Kopp *et al.* 2000), the Makran accretionary prism is formed due to the subduction of the Arabian plate beneath southern Iran and Pakistan. The convergence rate between Arabia and eastern Iran/western Pakistan varies from $19.5 \pm 2\,\mathrm{mm\,yr^{-1}}$ in the west to $27 \pm 2\,\mathrm{mm\,yr^{-1}}$ in the east (Vernant *et al.* 2004). Accretion of sediment into the wedge is thought to have started in the Eocene (Byrne *et al.* 1992), however, an imbricate zone of upper Cretaceous rocks have been identified in the northern part of the Makran (Dolati 2010), which may represent the onset of sediment accretion. These observations give a possible age range for the onset of growth of the accretionary wedge of 30–90 Myr.

Fig. 5(b) shows three topographic profiles across the Makran centred on 59.5ºE, 61ºE and 63ºE (red, green and blue lines, respectively). The profiles show a negligible along-strike change in topography suggesting a 2-D model is appropriate. Fig. 5(c) plots the sediment–basement interface from seismic reflection profiles at 62.9ºE (the solid black line; Kopp *et al.* 2000). The blue dots plot the inferred subduction interface at 62ºE (Penney *et al.* 2017) based on the location of earthquakes interpreted as occurring on the subduction interface or within the subducting plate. In the following comparisons, we take the middle topographic profile at 61ºE (as there is negligible along strike variation) along with the sediment–basement and plate interface data sets shown in Fig. 5(c). We assume the backstop of the wedge is located roughly at 27.5ºN based on the location of the Jaz Murian and Maskel depressions, which low elevations and low seismic strain rates suggest are relatively undeformed. However, we will show that the position of the backstop only affects the age of the wedge in the numerical simulations, and not our overall conclusions regarding the controls on the evolution of the wedge.

We consider the effects of flexure in the Makran accretionary prism by calculating two models with different elastic thicknesses, but with the same incoming sediment thickness, viscosity and density, underlying mantle density and underthrusting plate convergence rate. First, we consider a flexural model with incoming sediment thickness $T_\mathrm{s} = 7 \pm 1\,\mathrm{km}$, convergence velocity $U = 25 \pm 5\,\mathrm{mm\,yr^{-1}}$ and mantle density $\rho_\mathrm{m} = 3300\,\mathrm{kg\,m^{-3}}$. We then find an elastic thickness, viscosity, density and age that best reproduces the observed topography and sediment–basement interface from 195 numerical simulations for different values of non-dimensional sediment thickness H_∞. For all input parameters, we failed to reproduce observations from the Makran accretionary prism for small sediment densities, suggesting significant sediment compaction. Hence, we take a higher estimate of $\lambda = 5.0$, $\rho = 2750\,\mathrm{kg\,m^{-3}}$.

For the range of sediment thicknesses and convergence rates, we find a good fit to the observations for an elastic thickness of $T_\mathrm{e} = 18$–$24\,\mathrm{km}$ (flexural parameter $l_\mathrm{e} = 56$–$69\,\mathrm{km}$) with incoming sediment viscosity $\eta = 0.9 - 1.5 \times 10^{20}\,\mathrm{Pa\,s}$ and an age of $t = 44$–$66\,\mathrm{Myr}$, given by parameters $H_\infty = 0.68 - 0.95$, $\Lambda_\mathrm{C} = 0.094 - 0.25$. A comparison between the numerical simulation and the observations for $T_\mathrm{s} = 7\,\mathrm{km}$ and $U = 25\,\mathrm{mm\,yr^{-1}}$ is plotted in Fig. 6(c) giving $T_\mathrm{e} = 20\,\mathrm{km}$, $\eta = 1.1 \times 10^{20}\,\mathrm{Pa\,s}$ and $t = 42\,\mathrm{Myr}$. The critical non-dimensional parameter $\Lambda_\mathrm{C} = \pi^{1/2} H_\infty^3/(1+\lambda) = 0.094$–$0.25 \ll 1$ suggests that the Makran accretionary prism evolved along Path 2 where vertical thickening was the dominant growth mechanism, although testing this hypothesis would require tectonic reconstructions beyond the scope of this study. The lateral extent and topographic height of the Makran accretionary prism are plotted on the regime plot in Fig. 2 given by the black hexagram labelled ‘M’ and shows that the Makran is now in the late-time regime. As a result, only the nose region of the sediment–basement interface, where flexure is important, can constrain the elastic thickness. Therefore, a wide range of elastic thicknesses, $T_\mathrm{e} = 18$–$24\,\mathrm{km}$, can fit the observations. Such elastic thicknesses are consistent with previous studies on the elastic thickness of the Arabian plate in the Makran zone (Chen *et al.* 2015), and with observed elastic thicknesses for oceanic lithosphere elsewhere (Craig & Copley 2014). Our estimate of the sediment viscosity is slightly higher than estimated previously in some studies (Emerman & Turcotte 1983; Shreve & Cloos 1986) but similar to other recent studies of viscous wedges (Medvedev 2002; Copley & McKenzie 2007). Finally, the estimated age of $t = 44$–$66\,\mathrm{Myr}$ is consistent with the geology but is primarily a function of the choice of location of the backstop, and hence volume of sediment accumulated in the wedge. As the wedge is in the late-time regime, the topographic height and plate deflection are given by eqs (31) and (19), which do not explicitly depend on time, although there is an implicit time dependence through lateral extent x_N. As a result, the choice of backstop location determines the age of the wedge but not any other parameter in the model.

The second model we consider is in isostatic balance ($T_\mathrm{e} = 0\,\mathrm{km}$), but otherwise has the same parameter values as the model described above. Fig. 6(a) plots the numerical profiles for the topographic height and base of the sediment with elastic thicknesses $T_\mathrm{e} = 0\,\mathrm{km}$ in isostatic balance (the solid red lines) and $T_\mathrm{e} = 20\,\mathrm{km}$ (the solid blue lines) for $t = 10, 20, 30, 40$ and $50\,\mathrm{Myr}$. The topography is almost identical in the two models, apart from the flexural depression and bulge at the nose of the wedge observed in the flexural model. However, there is a significant difference between the two models in the depth to the base of the sediment, particularly behind the nose where the dip of the base of the sediment is much more gentle in the flexural model compared with the isostatic model. Figs 6(b) and (c) then compare these models for $t = 42\,\mathrm{Myr}$ in each case, with the data for the topographic height and sediment–basement interface (the solid black lines with the open circles). The topography agrees well in both cases. When considering the base of the sediment, particularly the comparison with the seismic reflection profiles, a flexural model with elastic thickness $T_\mathrm{e} = 20\,\mathrm{km}$ does a better job at reproducing the observed geometry than the purely isostatic model where the elastic thickness is neglected. This result suggests that flexure is necessary to explain the dipping sediment–basement interface as observed in seismic reflection profiles, and hence shows the importance of modelling flexure in the underlying plate.

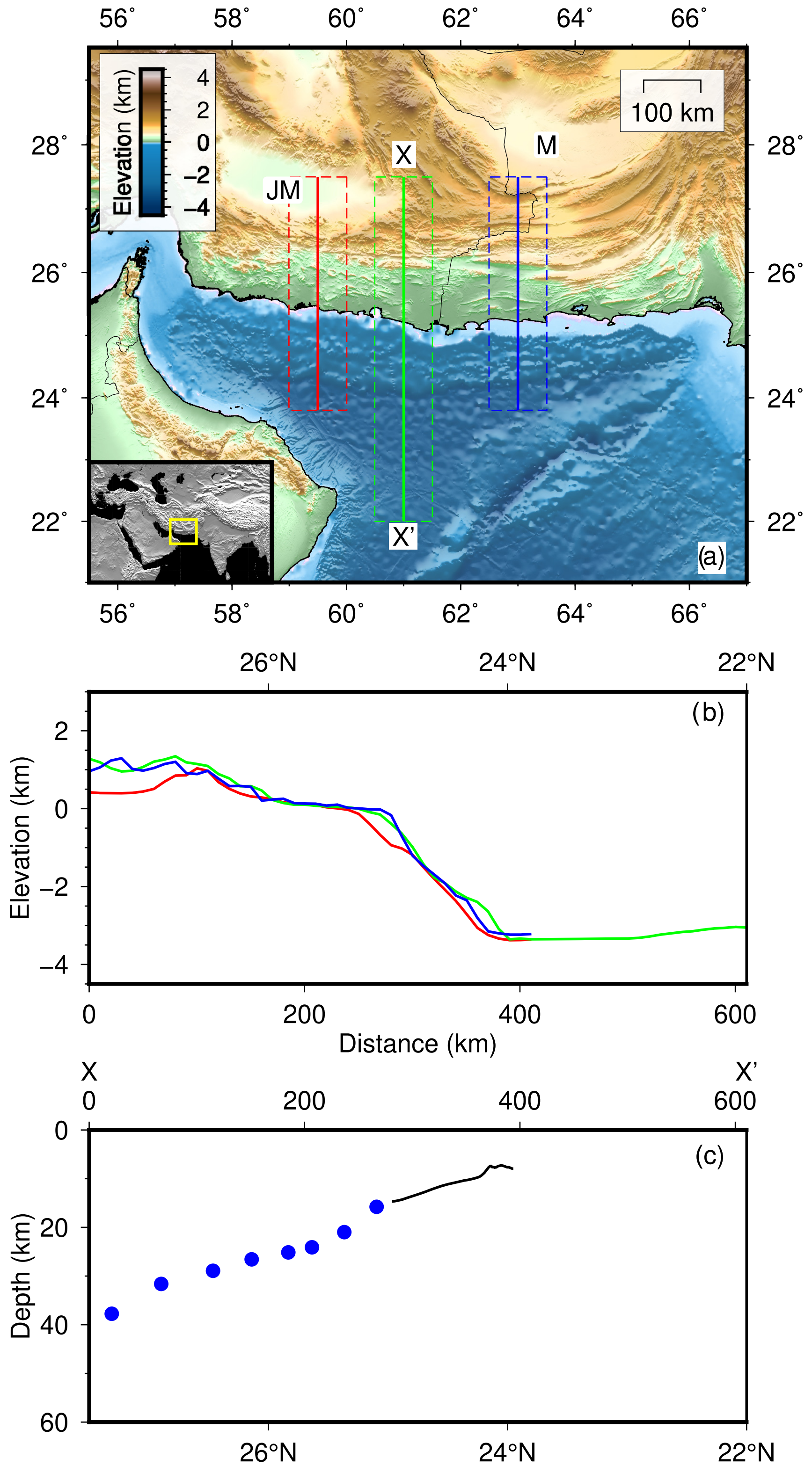

Figure 5. (a) Map of the Makran with cross-sections at 59.5°E, 61°E and 63°E marked by the red, green and blue boxes, respectively. The dashed lines indicate the region over which profile is averaged. The Jaz Murian and Maskel depressions are marked by 'JM' and 'M'. (b) Averaged topographic profiles using a 10 km Gaussian filter plotted from north to south. (c) Sediment–basement interface from seismic reflection data at 62.9°E (the solid black line; Kopp *et al.* 2000) and inferred subduction interface at 62°E (Penney *et al.* 2017) based on the location of earthquakes interpreted as occurring on the subduction interface or within the subducting plate (the blue dots).

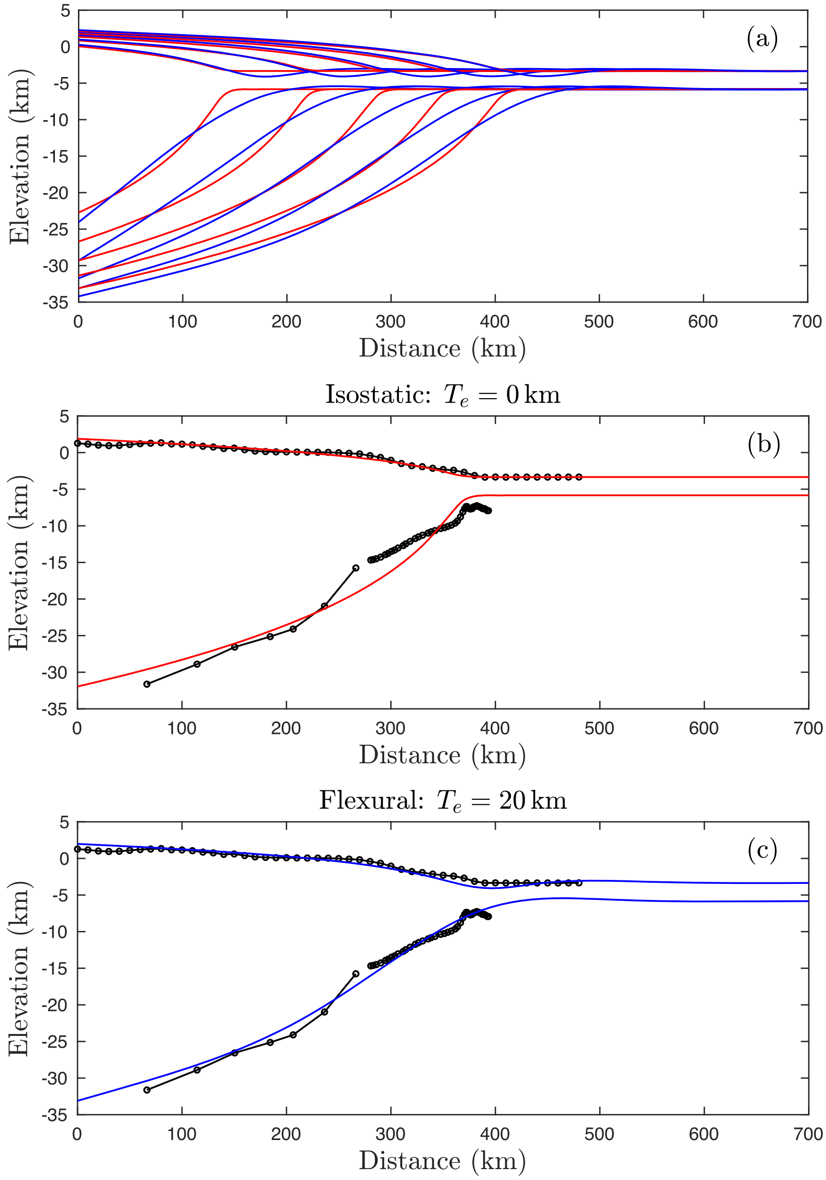

Figure 6. (a) Numerical profiles of the topography and sediment–basement interface for isostatic model with $T_\mathrm{e} = 0\,\mathrm{km}$ (the red lines) and flexural model with $T_\mathrm{e} = 20\,\mathrm{km}$ (the blue lines) for $t = 10$, 20, 30, 40 and 50 Myr. (Sediment thickness $T_\mathrm{s} = 7\,\mathrm{km}$, convergence velocity $U = 25\,\mathrm{mm\,yr^{-1}}$, viscosity $\eta = 1.1 \times 10^{20}\,\mathrm{Pa\,s}$, and sediment and underlying mantle densities $\rho = 2750\,\mathrm{kg\,m^{-3}}$, $\rho_\mathrm{m} = 3300\,\mathrm{kg\,m^{-3}}$, density ratio $\lambda = 5.0$). (b) Isostatic model with $T_\mathrm{e} = 0\,\mathrm{km}$ for $t = 42$ Myr (the red line) plotted against data for topography and sediment–basement interface (the solid black line with the open circles). (c) Flexural model with $T_\mathrm{e} = 20\,\mathrm{km}$ for $t = 42$ Myr (the blue line) plotted against data for topography and sediment–basement interface (the solid black line with the open circles).

5.2 Indo–Burman Ranges

The Indo–Burman Ranges were formed by accretion of sediment from the underthrusting Indian plate as it subducts beneath southeast Asia (Ni *et al.* 1989; Stork *et al.* 2008; Steckler *et al.* 2016), see Fig. 7(a). The fold-thrust belt is thought to have developed since the late Oligocene (Soibam *et al.* 2015). Two topographic sections, north and south of the Shillong Plateau (marked as ‘SP’ in Fig. 7a), are shown in Fig. 7 as the blue and red lines. The surface geology within the Indo–Burman Ranges is characterized by progressively older rocks from west to east. South of the Shillong Plateau, sedimentary rocks in the central part of the range are composed of an Eocene sequence, ‘inner’ Indo–Burman wedge, with a western portion of younger rock composed of Neogene fluvio-deltaic sediments and turbidites, ‘outer’ Indo–Burman wedge (Sikder & Alam 2003; Khin *et al.* 2014, 2017). The eastern margin of the Indo–Burman Range is characterized by upper-Cretaceous and Triassic deep water sediments, Mesozoic metamorphics and Jurassic ophiolite assemblages (Brunnschweiler 1974; Mitchell 1993). North of the Shillong Plateau, the western portion of the Indo–Burman wedge comprises of an Oligocene sedimentary sequence, with a region towards the east of Cretaceous sandstones overlying mafic volcanics of a Jurassic ophiolite suite (Brunnschweiler 1966; Ghose & Singh 1980). The region of ophiolites and metamorphics that straddle the length of the range is taken to represent a rigid backstop, which allows the fold-thrust belt to form (marked in Fig. 7a, the black dashed line; Figs 7b and c, the grey shaded region).

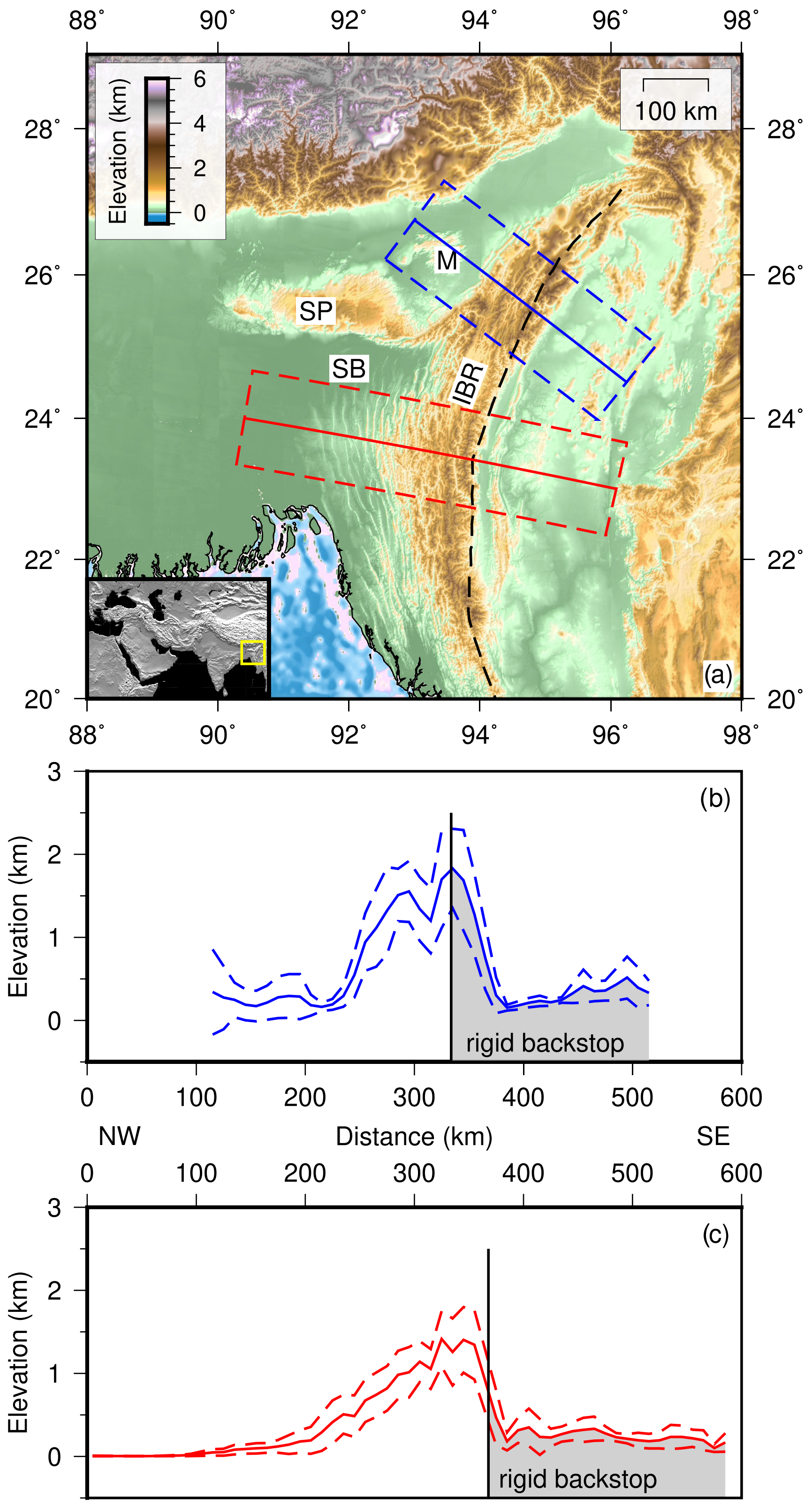

Figure 7. (a) Map of the Indo–Burman Ranges with cross-sections through the northern (the blue line) and southern (the red line) portion of the range. The dashed lines indicate the region over which the profile is averaged. The Shillong Plateau is marked by ‘SP’, the Mikir Hills by ‘M’ and the Surma Basin by ‘SB’. Estimate of location of the backstop given by the black dashed line. (b) Averaged topographic profile using a 10 km Gaussian filter along the northern cross-section (the blue line) with error bar of one standard deviation. The grey shaded area indicates estimate of the backstop. (c) Same as (b) for the southern cross-section.

Along the Indo–Burman Ranges from north to south of the Shillong Plateau, there is a significant change in both foreland sediment thickness and the topography of the wedge. In the north, the Indo–Burman Ranges are bounded to the west by the lowlands of Assam. The sediment thickness ranges from zero, where the crystalline basement is exposed at the surface (e.g. Mikir Hills, marked as 'M' in Fig. 7a), up to ∼5 km (Dasgupta *et al.* 2000) in the northeastern corner of the syntaxis. The average shown by Dasgupta *et al.* (2000) is ∼ 2 km. The topography is characterized by a narrow range width and steep surface slopes near the range front, shown as the blue lines in Fig. 7(b). South of the Shillong Plateau, the Indo–Burman Ranges are bounded by the Surma Basin (marked as 'SB' in Fig. 7a) and the Bengal Basin, where the sediment thickness in the foreland is significantly larger (∼15–22 km; Curray 1991; Alam *et al.* 2003). The Indo–Burman Range has a larger width and shallower surface slopes than to the north of the Shillong Plateau, shown as the red lines in Fig. 7(c).

The sedimentary sequences that make up the fold-thrust belt to the west of the backstop in the Indo–Burman Ranges were originally deposited in a series of basins with a common sediment source from the Ganges and Brahmaputra river networks (Steckler *et al.* 2008; Govin *et al.* 2018). Hence, we expect the lithology of the sediment in the north and south Indo–Burman wedge to be similar. This similarity suggests that this region may provide insights into the effects of changing sediment thickness on the formation of a fold-thrust belt.

The lower–crustal depth and strike-slip style of earthquakes in the Indo–Burman Ranges suggest they are occurring within the underthrusting Indian plate (Mitra *et al.* 2005). Hence, the earthquake locations do not constrain the depth of the thrust interface. In the analysis to follow, we, therefore, focus on the geometry of topography in the region, rather than the (unknown) geometry of the underthrusting plate.

The Indo–Burman Ranges have shallower surface slopes and larger range widths where the foreland sediment thickness is larger, south of the Shillong Plateau. This observation is consistent with the effect of increasing sediment thickness shown in Fig. 4. To investigate further, we consider two models in isostatic balance with different incoming sediment thicknesses, but otherwise the same parameter values. We assume isostatic balance as we do not have information about the underthrusting plate needed to constrain the elastic thickness. However, as shown in Fig. 4, the qualitative behaviour of changing sediment thickness is independent of the elastic thickness, and hence this does not affect our conclusions. We consider a range of sediment densities $\rho = 2400–2750\,\mathrm{kg\,m^{-3}}$, with mantle density $\rho_\mathrm{m} = 3300\,\mathrm{kg\,m^{-3}}$ (density ratio $\lambda = 2.7-5.0$). We then find the viscosity, convergence velocity and sediment thicknesses in the north and south that best reproduce the observations of topography. From the estimate that the formation of the fold-thrust belt started in the Oligocene (Soibam *et al.* 2015), we take an age of $t = 30 \pm 10$ Myr. However, this choice only affects the quantitative parameter values determined, not the qualitative interpretations. For the estimated range of ages and sediment densities, we find incoming sediment thickness in the north of $T_\mathrm{s(north)} = 2.1–2.3$ km and in the south of $T_\mathrm{s(south)} = 4.7–5.0$ km, with sediment viscosity $\eta = 3.0 - 8.8 \times 10^{19}$ Pa s and underthrusting plate convergence velocity $U = 2.8–8.8\,\mathrm{mm\,yr^{-1}}$ for both the north and the south.

The estimate of incoming sediment thickness in the north is consistent with the observation that the foreland sediment thickness can range from 0 to ∼5 km in places (Dasgupta *et al.* 2000) with an average of ∼2 km. In the south, however, the estimate of $T_\mathrm{s(south)} = 4.7–5.0$ km is significantly less than the observation ∼15–22 km from seismic data (Curray 1991; Alam *et al.* 2003). It has been suggested that temperatures and pressures at large depths in the sediment layer are sufficient for metamorphism to take place (Curray 1991). If this is the case, only the upper deformable portions of the sediment layer may be playing a role in the growth of the wedge. Given that our model estimates the effective deformable sediment thickness, we would expect to underestimate the true sediment thickness, as the deeper parts will be dewatered, lithified, and effectively part of the rigid Indian plate. Crucially, our models reproduce a thicker sediment sequence to the south than north of the Shillong Plateau, consistent with the observations. Sikder & Alam (2003) observe a detachment in seismic reflection data at around 4 s two-way traveltime, corresponding with a depth of roughly ∼5 km, which is consistent with more recent studies (Betka *et al.* 2018), and hence supports our estimate of the effective deformable sediment thickness. The value of sediment viscosity $\eta = 3.0 - 8.8 \times 10^{19}$ Pa s is consistent with previous studies on the Indo–Burman Ranges (Copley & McKenzie 2007) and on sediments under similar conditions (Nino *et al.* 1998; Gratier *et al.* 1999; Connolly & Podladchikov 2000). Finally, the convergence velocity of $U = 2.8–8.8\,\mathrm{mm\,yr^{-1}}$ is consistent with the total rate of convergence of $5–10\,\mathrm{mm\,yr^{-1}}$ in this area from present-day geodetic data (Steckler *et al.* 2016), but we note there is a trade-off with estimating the age of the fold-thrust belt, the sediment volume and changes in either of these quantities through time.

Fig. 8(a) plots numerical profiles for the topographic height of a wedge with sediment thicknesses $T_\mathrm{s(north)} = 2.2$ km (the solid blue lines) and $T_\mathrm{s(south)} = 5.0$ km (the solid red lines) for $t = 10,\ 20,\ 30,\ 40$ and 50 Myr, with convergence velocity $U = 3.8\,\mathrm{mm\,yr^{-1}}$, viscosity $\eta = 5.0 \times 10^{19}$ Pa s, and sediment and underlying mantle densities $\rho = 2400\,\mathrm{kg\,m^{-3}}$, $\rho_\mathrm{m} = 3300\,\mathrm{kg\,m^{-3}}$. This comparison again shows that for larger sediment thicknesses, the wedge formed has a larger range width with a shallower topographic slope. Figs 8(b) and (c) plot the comparisons between topographic data in the northern and southern part of the Indo–Burman Ranges, respectively (the solid black lines with the open circles) with the numerical profiles for an age of $t = 30$ Myr (the blue and red solid lines). By increasing the sediment thickness by more than a factor of 2 going from the north to the south, the difference in surface slopes and range widths can be reproduced. The discrepancy in Fig. 8(b) between the back of the wedge in the numerical simulation and the backstop inferred from the geology is due to choosing the same age for the fold-thrust belt in the north and south. However, the mismatch between the observations and the model is small given the uncertainties in the location of the backstop. Our results, therefore, suggest that the incoming sediment thickness is playing a first-order role in the development of topography in the Indo–Burman Ranges.

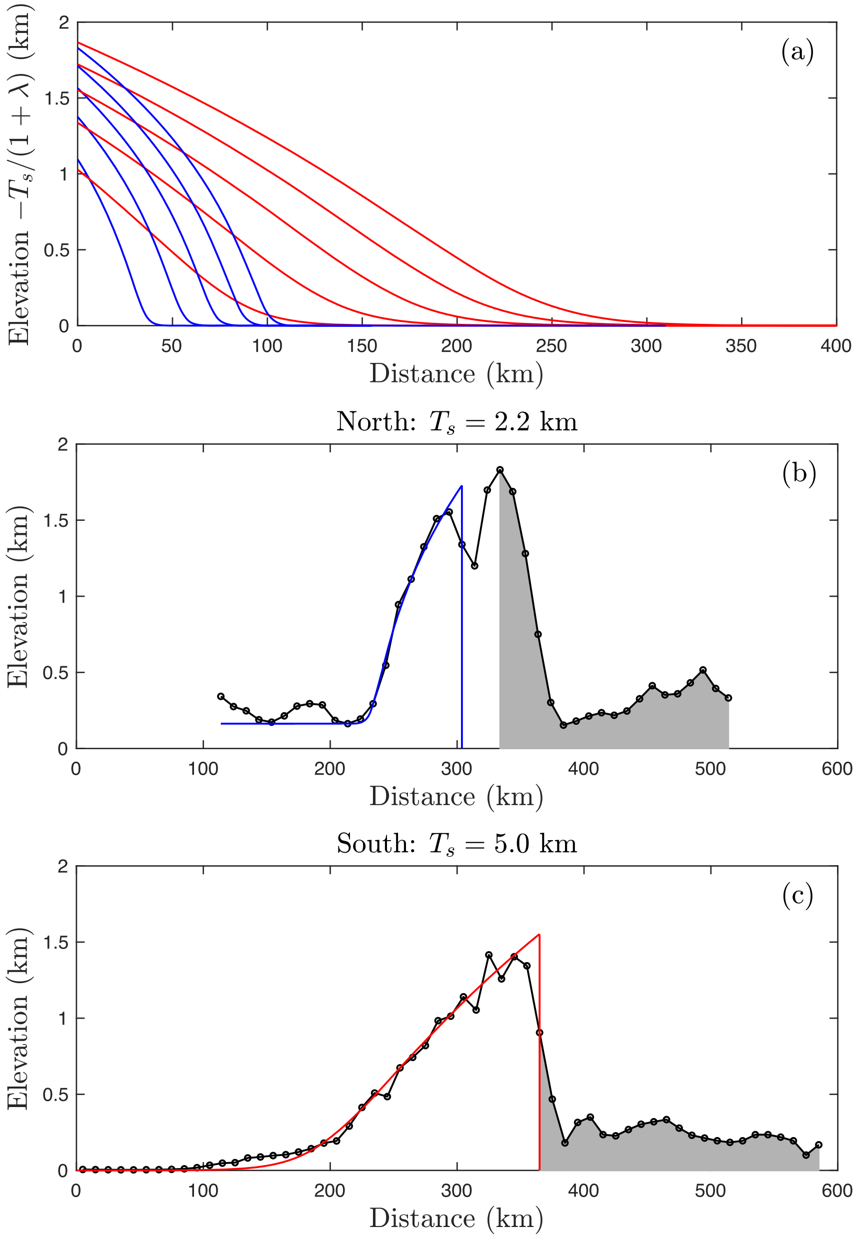

Figure 8. (a) Numerical profiles of the topography for sediment thicknesses $T_{\mathrm{s(north)}} = 2.2$ km (the solid blue lines) and $T_{\mathrm{s(south)}} = 5.0$ km (the solid red lines) for $t = 10, 20, 30, 40$ and 50 Myr. (Convergence velocity $U = 3.8\,\mathrm{mm\,yr^{-1}}$, viscosity $\eta = 5.0 \times 10^{19}$ Pa s, and sediment and underlying mantle densities $\rho = 2400\,\mathrm{kg\,m^{-3}}$, $\rho_{\mathrm{m}} = 3300\,\mathrm{kg\,m^{-3}}$, density ratio $\lambda = 2.7$.) (b) Numerical profile with $T_{\mathrm{s(north)}} = 2.2$ km for $t = 30$ Myr (the solid blue line) plotted against topographic data for northern cross-section of Indo–Burman Range (the solid black line with the open circles). (c) Numerical profile with $T_{\mathrm{s(south)}} = 5.0$ km for $t = 30$ Myr (the solid red line) plotted against topographic data for southern cross-section of Indo–Burman Range (the solid black line with the open circles). All models are in isostatic balance with $T_{\mathrm{e}} = 0$ km.

5.3 Comparison with Coulomb wedge theory

In our model, we use a purely viscous rheology to describe the incoming sediment. As a result of this choice of rheology, the shear stresses are unbound. The shear stress can be written as

$$\tau = \eta \frac{\partial u}{\partial z} = -\rho g \frac{\partial h}{\partial x}(h - z), \tag{33}$$

which is maximum at the base, $z = s$. For example, for the flexural model proposed for the Makran shown in Fig. 6(c), the maximum shear stress at the base is ∼8 MPa, in agreement with that calculated by Penney *et al.* (2017) of ∼5–35 MPa. For the Indo–Burman Ranges, the maximum shear stress is calculated for the base of northern profile, shown in Fig. 8(b), to be ∼1 MPa. Hence, for both comparisons the shear stress is low, and is consistent with the levels of stress under which rocks can deform at geological strain rates by creep. Unlike Coulomb wedge theory that includes a yield stress, our model does not aim to explain brittle deformation. For a purely viscous rheology, the strain rate is linearly proportional to the shear stress, $\dot{\xi} = \tau/\eta$. Eq. (33) shows that the strain rate increases linearly with depth and is proportional to gradients in surface topography. At late times, the topography of our model wedges exhibits concave-downward profiles with increasing surface gradients towards the toe of the wedge. Hence, we would expect to see the largest strain-rates at depth and towards the toe; a feature analogous to the strain rate pattern for Coulomb wedge theory as described by Willett (1992).

A key feature of Coulomb wedge theory is that everywhere in the interior of the wedge is on the verge of failure by the same mechanism, that is, thrust faulting at the angle of sliplines. In contrast, our model allows for distributed and spatially variable deformation. The main distinguishing feature between our viscous model and Coulomb wedge theory is the surface topography of wedges produced. Unlike the linear taper from cohesionless Coulomb wedge theory, a viscous rheology produces a range of topographies from concave upward to concave downward as the wedge evolves in time. As seen from the comparisons with the Makran accretionary prism and the Indo–Burman Ranges, these shapes are consistent with observations from a range of locations. However, a clear direction for future work will be to examine the extent to which this is globally true.

6 CONCLUSIONS

We have presented an analytical and numerical model to describe the growth of a fold-thrust belt due to the accretion of sediments from the underthrusting plate. In particular, we have examined a balance between advection of sediment and gravitational spreading within an accretionary wedge coupled to the flexural subsidence of the underthrusting plate. Our analysis shows that the evolution of accretionary wedges is crucially dependent on two non-dimensional parameters: the non-dimensional sediment thickness $H_\infty = T_s(\rho g/3\eta U l_e)^{1/3}$ and the density ratio $\lambda = \rho/\Delta\rho$, where T_s, ρ, η are the incoming sediment thickness, density and viscosity, U is the convergence rate of the incoming plate and l_e is the flexural parameter, the length scale at which the weight of the wedge begins to dominate over the strength of the plate. We describe early- and late-time regimes of the wedge and demonstrate two paths of evolution between these regimes, where the wedge either grows predominantly through gravitational spreading (Path 1) or through vertical thickening due to advection of sediment (Path 2) depending on the size of the critical non-dimensional parameter $\Lambda_C = \pi^{1/2} H_\infty^3/(1+\lambda)$. In addition, we solve the coupled system numerically to understand the transition between these regimes and explore the parameter space more widely.

The generality of our model allows conclusions to be drawn in a multitude of locations. We have considered the particular examples of the Makran accretionary prism and the Indo–Burman Ranges, to investigate the importance of sediment thickness and elastic thickness (flexure of the underthrusting plate) in the growth of a fold-thrust belt. We have shown that flexure is important in the Makran accretionary prism in order to understand dip in the sediment–basement interface from seismic reflections profiles. In the Indo–Burman Ranges, we have shown that a lateral contrast in sediment thickness plays an important role in generating the different styles of topography north and south of the Shillong Plateau.

ACKNOWLEDGEMENTS

The authors would like to thank Gregory Houseman and an anonymous reviewer for helpful comments that improved the manuscript. TVB was funded by an NERC studentship. CEP was funded by an NERC studentship and Junior Research Fellowship from Queens' College, Cambridge. JAN was supported by a Royal Society University Research Fellowship. ACC was partly supported by the NERC large grant 'Looking Inside the Continents from Space'. Some figures were prepared using the GMT package (Wessel *et al.* 2013).

REFERENCES

Alam, M., Alam, M.M., Curray, J.R., Chowdhury, M.L.R. & Gani, M.R., 2003. An overview of the sedimentary geology of the Bengal Basin in relation to the regional tectonic framework and basin-fill history, *Sedimentary Geol.,* **155**(3–4), 179–208.

Beaumont, C., Jamieson, R.A., Nguyen, M.H. & Lee, B., 2001. Himalayan tectonics explained by extrusion of a low-viscosity crustal channel coupled to focused surface denudation, *Nature,* **414**(6865), 738–742.

Betka, P.M., Seeber, L., Thomson, S.N., Steckler, M.S., Sincavage, R. & Zoramthara, C., 2018. Slip-partitioning above a shallow, weak décollement beneath the Indo–Burman accretionary prism, *Earth planet. Sci. Lett.,* **508,** 17–28.

Borja, R.I. & Dreiss, S.J., 1989. Numerical modeling of accretionary wedge mechanics: application to the Barbados subduction problem, *J. geophys. Res.,* **94**(B7), 9323–9339.

Brace, W.F. & Kohlstedt, D.L., 1980. Limits on lithospheric stress imposed by laboratory experiments, *J. geophys. Res.,* **85**(B11), 6248–6252.

Brunnschweiler, R.O., 1966. On the geology of the Indo–Burman Ranges, *J. Geol. Soc. Aust.,* **13,** 137–194.

Brunnschweiler, R.O., 1974. Indo–Burman Ranges, *Geol. Soc. Spec. Publ.,* **4,** 279–299.

Burov, E.V., Kogan, M.G., Lyon-Caen, H. & Molnar, P., 1990. Gravity anomalies, the deep structure, and dynamic processes beneath the Tien Shan, *Earth planet. Sci. Lett.,* **96,** 367–383.

Byrne, D.E., Sykes, L.R. & Davis, D.M., 1992. Great thrust earthquakes and aseismic slip along the plate boundary of the makran subduction zone, *J. geophys. Res.,* **97**(B1), 449–478.

Chapple, W.M., 1978. Mechanics of thin-skinned fold-and-thrust belts, *Bull. Geol. Soc. Am.,* **89**(8), 1189–1198.

Chen, B., Kaban, M.K., Khrepy, S.E. & Al-Arifi, N., 2015. Effective elastic thickness of the arabian plate: weak shield versus strong platform, *Geophys. Res. Lett.,* **42**(2), 7623–7932.

Chen, W.-P. & Molnar, P., 1983. Focal depths of intracontinental and intraplate earthquakes and their implications for the thermal and mechanical properties of the lithosphere, *J. geophys. Res.,* **88**(B5), 4183–4214.

Connolly, J.A.D. & Podladchikov, Y.Y., 2000. Temperature-dependent viscoelastic compaction and compartmentalization in sedimentary basins, *Tectonophysics,* **324**(3), 137–168.

Copley, A. & McKenzie, D., 2007. Models of crustal flow in the India-Asia collision zone, *Geophys. J. Int.,* **169**(2), 683–698.

Craig, T.J. & Copley, A., 2014. An explanation for the age independence of oceanic elastic thickness estimates from flexural profiles at subduction zones, and implications for continental rheology, *Earth planet. Sci. Lett.,* **392,** 207–216.

Curray, J.R., 1991. Possible greenschist metamorphism at the base of a 22-km sedimentary section, Bay of Bengal, *Geology,* **19**(11), 1097–1100.

Dahlen, F.A., 1984. Noncohesive critical Coulomb wedges: an exact solution, *J. geophys. Res.,* **89**(B12), 10 125–10 133.

Dahlen, F.A., 1990. Critical taper model of fold-and-thrust belts and accretionary wedges, *Annu. Rev. Earth Planet. Sci.,* **18**(1), 55–99.

Dahlen, F.A., Suppe, J. & Davis, D., 1984. Mechanics of fold-and-thrust belts and accretionary wedges: cohesive Coulomb theory, *J. geophys. Res.,* **89**(B12), 10 087–10 101.

Dasgupta, S., Narula, P., Acharyya, S. & Banerjee, J., 2000. Seismotectonic atlas of India and its environs, *Geol. Surv. India*.

Davis, D., Suppe, J. & Dahlen, F.A., 1983. Mechanics of fold-and-thrust belts and accretionary wedges, *J. geophys. Res.,* **88**(B2), 1153–1172.

Dolati, A., 2010. Stratigraphy, structural geology and low-temperature thermochronology across the Makran accretionary wedge in Iran, *PhD thesis,* Swiss Institute of Technology Zurich.

Elliot, D., 1976. The motion of thrust sheets, *J. geophys. Res.,* **81**(5), 949–963.

Ellis, S., Fullsack, P. & Beaumont, C., 1995. Oblique convergence of the crust driven by basal forcing: implications for length–scales of deformation and strain partitioning in orogens, *Geophys. J. Int.,* **120**(1), 24–44.

Emerman, S.H. & Turcotte, D.L., 1983. A fluid model for the shape of accretionary wedges, *Earth planet. Sci. Lett.,* **63**(3), 379–384.

England, P. & McKenzie, D., 1982. A thin viscous sheet model for continental deformation, *Geophys. J. R. astr. Soc.,* **53**(9), 1689–1699.

Flesch, L., Bendick, R. & Bischoff, S., 2018. Limitations on inferring 3D architecture and dynamics from surface velocities in the India-Eurasia collision zone, *Geophys. Res. Lett.,* **45,** 1379–1386.

Forsyth, D.W., 1985. Subsurface loading and estimates of the flexural rigidity of continental lithosphere, *J. geophys. Res.,* **90**(B14), 12 623–12 632.

Ghose, N.C. & Singh, R.N., 1980. Occurrence of blueschist facies in the ophiolite belt of Naga Hills, East of Kiphire, N. E. India, *Geol. Rundsch.,* **69,** 41–48.

Govin, G., Najman, Y., Copley, A., Millar, I., van der Beek, P., Huyghe, P., Grujic, D. & Davenport, J., 2018. Timing and mechanism of the rise of the Shillong plateau in the Himalayan foreland, *Geology,* **46**(3), 279–282.

Gratier, J.-P., Renard, F. & Labaume, P., 1999. How pressure solution creep and fracturing processes interact in the upper crust to make it behave in both a brittle and viscous manner, *J. Struct. Geol.,* **21**(8-9), 1189–1197.

Gratton, J. & Perazzo, C.A., 2009. Self-similar asymptotics in convergent viscous gravity currents of non-newtonian liquids, *J. Phys.: Conf. Ser.,* **166,** 012011.

Haddad, D. & Watts, A.B., 1999. Subsidence history, gravity anomalies, and flexure of the Northeast Australian margin in Papua New Guinea, *Tectonics,* **18**(5), 827–842.

Jordan, T.A. & Watts, A.B., 2005. Gravity anomalies, flexure and the elastic thickness structure of the India-Eurasia collisional system, *Earth planet. Sci. Lett.,* **236**(3-4), 732–750.

Karner, G.D. & Watts, A.B., 1983. Gravity anomalies and flexure of the lithosphere at mountain ranges, *J. geophys. Res.,* **88**(B12), 10 449–10 477.

Khin, K., Sakai, T. & Zaw, K., 2014. Neogene syn-tectonic sedimentation in the eastern margin of Arakan-Bengal Basins, and its implications on for the Indian-Asian collision in Western Myanmar, *Gondwana Res.,* **26**(1), 89–111.

Khin, K., Sakai, T. & Zaw, K., 2017. Arakan coastal ranges in Western Myanmar, geology and provenance of neogene siliciclastic sequences: implications for the tectonic evolution of the Himalaya-Bengal System, *Geol. Soc. Mem.,* **48,** 81–116.

Kopp, C., Fruehn, J., Flueh, E.R., Reichert, C., Kukowski, N., Bialas, J. & Klaeschen, D., 2000. Structure of the Makran subduction zone from wide-angle and reflection seismic data, *Tectonophysics,* **329**(1-4), 171–191.

Lyon-Caen, H. & Molnar, P., 1983. Constraints on the structure of the Himalaya from an analysis of gravity anomalies and a flexural model of the lithosphere, *J. geophys. Res.,* **88**(B10), 8171–8191.

Mandl, G., 1988. Mechanics of tectonic faulting: models and basic concepts, *Dev. Struct. Geol. I,* **1,** 407.

McKenzie, D. & Fairhead, D., 1997. Estimates of the effective elastic thickness of the continental lithosphere from Bouguer and free air gravity anomalies, *J. geophys. Res.,* **102**(B12), 27523–27552.

Meade, B.J., 2007. Present-day kinematics at the India-Asia collision zone, *Geology,* **35**(1), 81–84.

Medvedev, S., 2002. Mechanics of viscous wedges: modeling by analytical and numerical approaches, *J. geophys. Res.,* **107**(B6), 2123.

Mitchell, A.H.G., 1993. Cretaceous-cenozoic tectonic events in the Western Myanmar (Burma)-Assam region, *J. Geol. Soc.,* **150**(6), 1089–1102.

Mitra, S., Priestley, K., Bhattacharyya, A.K. & Gau, V.K., 2005. Crustal structure and earthquake focal depths beneath Northeastern India and Southern Tibet, *Geophys. J. Int.,* **160**(1), 227–248.

Molnar, P. & Tapponnier, P., 1975. Cenozoic tectonics of Asia: effects of a continental collision, *Science,* **189**(4201), 419–426.

Ni, J.F., Guzman-Speziale, M., Bevis, M., Holt, W.E., Wallace, T.C. & Seager, W.R., 1989. Accretionary tectonics of Burma and the three-dimensional geometry of the Burma subduction zone, *Geology,* **17**(1), 68–71.

Nino, F., Chéry, J. & Gratier, J.-P., 1998. Mechanical modeling of compressional basins: origin and interaction of faults, erosion, and subsidence in the Ventura basin, California, *Tectonics,* **17**(6), 955–972.

Penney, C. *et al.*, 2017. Megathrust and accretionary wedge properties and behaviour in the Makran subduction zone, *Geophys. J. Int.,* **209**(3), 1800–1830.

Perazzo, C.A. & Gratton, J., 2008. Asymptotic regimes of ridge and rift formation in a thin viscous sheet model, *Phys. Fluids,* **20**(4), 043103.

Perazzo, C.A. & Gratton, J., 2010. Convergent flow in a two-layer system and mountain building, *Phys. Fluids,* **22**(5), 056603.

Price, R.A., 1973. Large-scale gravitational flow of supra-crustal rocks, Southern Canadian rockies, in *Gravity and Tectonics,* pp. 491–502, eds DeJong, K.A. & Scholten, R., John Wiley.

Ruh, J.B., Kaus, B.J. & Burg, J.P., 2012. Numerical investigation of deformation mechanics in fold-and-thrust belts: influence of rheology of single and multiple décollements, *Tectonics,* **31**(3), 1–23.

Rutter, E.H., 1983. Pressure solution in nature, theory and experiment, *J. Geol. Soc.,* **140,** 725–740.

Schlichting, H. & Shapiro, A. H., 1979. *Boundary-Layer Theory,* 7th edn, McGraw-Hill.

Shreve, R.L. & Cloos, M., 1986. Dynamics of sediment subduction, melange formation, and prism accretion, *J. geophys. Res.,* **91**(B10), 10229–10245.

Sikder, A.M. & Alam, M.M., 2003. 2-D modelling of the anticlinal structures and structural development of the eastern fold belt of the Bengal Basin, Bangladesh, *Sedimentary Geol.,* **155**(3-4), 209–226.

Simpson, G.D.H., 2006. Modelling interactions between fold-thrust belt deformation, foreland flexure and surface mass transport, *Basin Res.,* **18**(2), 125–143.

Simpson, G.D.H., 2010. Influence of the mechanical behaviour of brittle-ductile fold-thrust belts on the development of foreland basins, *Basin Res.,* **22**(2), 139–156.

Simpson, G.D.H., 2011. Mechanics of non-critical fold-thrust belts based on finite element models, *Tectonophysics,* **499**(1-4), 142–155.

Snyder, D.B. & Barazangi, M., 1986. Deep crustal structure and flexure of the Arabian plate beneath the Zagros collisional mountain belt as inferred from gravity observations, *Tectonics,* **5**(3), 361–373.

Soibam, I., Khuman, M.C. & Subhamenon, S.S., 2015. Ophiolitic rocks of the Indo-Myanmar Ranges, NE India: relicts of an inverted and tectonically imbricated hyper extended continental margin basin? *Geol. Soc. Spec. Publ.,* **413,** 301–331.

Steckler, M.S., Akhter, S.H. & Seeber, L., 2008. Collision of the Ganges-Brahmaputra delta with the Burma arc: implications for earthquake hazard, *Earth planet. Sci. Lett.,* **273**(3-4), 67–378.

Steckler, M.S., Mondal, D.R., Akhter, S.H., Seeber, L., Feng, L., Gale, J., Hill, E.M. & Howe, M., 2016. Locked and loading megathrust linked to active subduction beneath the Indo–Burman Ranges, *Nat. Geosci.,* **9**(8), 615–618.

Stockmal, G.S., 1983. Modeling of large-scale accretionary wedge deformation, *J. geophys. Res.,* **88**(B10), 8271–8287.

Stockmal, G.S., Beaumont, C., Nguyen, M.H. & Lee, B., 2007. Mechanics of thin-skinned fold-and-thrust belts: insights from numerical models, *Geol. Soc. Am.,* **433,** 63–98.

Stork, A.L., Selby, N.D., Heyburn, R. & Searle, M.P., 2008. Accurate relative earthquake hypocenters reveal structure of the Burma subduction zone, *Bull. seism. Soc. Am.,* **98**(6), 2815–2827.

Suppe, J., 1980. A retrodeformable cross-section of Northern Taiwan, *Proc. Geol. Soc. China,* **23,** 46–55.

Timoshenko, A. & Woinowsky-Krieger, S., 1959. *Theory of Plates and Shells,* McGraw-Hill.

Vernant, P. *et al.*, 2004. Present-day crustal deformation and plate kinematics in the middle east constrained by gps measurements in Iran and Northern Oman, *Geophys. J. Int.,* **157**(1), 381–398.

Walcott, R.I., 1970. Flexural rigidity, thickness, and viscosity of the lithosphere, *J. geophys. Res.,* **75**(20), 3941–3954.

Wang, K. & Hu, Y., 2006. Accretionary prisms in subduction earthquake cycles: the theory of dynamic Coulomb wedge, *J. geophys. Res.,* **111**(B06410).

Wang, W.-H., 2001. Lithospheric flexure under a critically tapered mountain belt: a new technique to study the evolution of the tertiary Taiwan orogeny, *Earth planet. Sci. Lett.,* **192**(4), 571–581.

Watts, A.B., Lamb, S.H., Fairhead, J.D. & Dewey, J.F., 1995. Lithospheric flexure and bending of the Central Andes, *Earth planet. Sci. Lett.,* **134**(1-2), 9–21.

Watts, A.B., Zhong, S.J. & Hunter, J., 2013. The behavior of the lithosphere on seismic to geologic timescales, *Annu. Rev. Earth Planet. Sci.,* **41,** 443–468.

Wessel, P., Smith, W.H.F., Scharroo, R., Luis, J.F. & Wobbe, F., 2013. Generic Mapping Tools: Improved version released, *EOS Transactions,* **9,** 409–410.

White, R.S., 1982. Deformation of the Makran accretionary sediment prism in the Gulf of Oman (North-West Indian Ocean), *Geol. Soc. Spec. Publ.,* **10,** 357–372.

Willett, S.D., 1992. Dynamic and kinematic growth and change of a Coulomb wedge, in *Thrust Tectonics,* pp. 19–31, ed. McClay, K.R., Chapman and Hall, London.

Zhao, W.-L., Davis, D.M., Dahlen, F.A. & Suppe, J., 1986. Origin of convex accretionary wedges: evidence from Barbados, *J. geophys. Res.,* **91**(B10), 10 246–10 258.